Applied Thermal Engineering 279 (2025) 127960

Contents lists available at ScienceDirect

Applied Thermal Engineering

journal homepage: www.elsevier.com/locate/apthermeng

Research Paper

Artificial intelligence – Numerical study of melting and solidification heat transfer in a bundle of petal tubes embedded in metal foam

Jana Shafi [a], Obai Younis [b], Saeed Tiari [c], Mohammad Ghalambaz [d,*]

[a] Department of Computer Engineering and Information, College of Engineering in Wadi Alddawasir, Prince Sattam Bin Abdulaziz University, Saudi Arabia
[b] Department of Mechanical Engineering, College of Engineering in Wadi Alddawasir, Prince Sattam Bin Abdulaziz University, Saudi Arabia
[c] Biomedical Engineering Department, Widener University, One University Pl, Chester, PA 19013, USA
[d] Department of Mathematical Sciences, Saveetha School of Engineering, SIMATS, Chennai, India

ARTICLE INFO

Keywords:
Melting and solidification heat transfer
Artificial neural networks
Artificial intelligence
Sustainability
Clean energy
Building energy storage

ABSTRACT

Maximizing energy efficiency is a topic of great interest to scientists and engineers. Energy recovery through thermal energy storage (LHTES) units is a promising technique that contributes to improving energy efficiency. The current article examines the thermal performance in petal-shaped tubes implanted in a metal foam-phase change material (PCM) domain using the local thermal non-equilibrium model. The enthalpy–porosity method was employed for phase transition. The impact of petal number, amplitude, and tube position on melting and solidification of PCM was analyzed by numerical simulations, resulting in a dataset of 161,000 records. These records were used to train the artificial neural network (ANN) in order to optimize the LHTES unit. The numerical findings indicated that the petal shape significantly improved the thermal performance of the system compared to the normal tube shape. It was also that petal number, amplitude, and tube position remarkably affect the thermal activities within the LHTES unit. Increasing the amplitude from 0.3 to 0.6 improved the melting and the solidification time by 13.6 and 16.2 %, respectively. The ANN models successfully captured complex thermal interactions, offering a powerful predictive tool for optimizing LHTES systems.

1. Introduction

Heat transfer is at the core of phase change material (PCM)–based thermal energy storage (TES) systems, where efficient melting and solidification directly determine the system's thermal performance and storage capacity. Despite PCMs offering high latent heat, their low thermal conductivity significantly limits heat transmission rates, prompting researchers to explore various enhancement strategies [1–3]. As reviewed by Leong et al. [1], the integration of fins, nanoparticles, and metal foams in triplex-tube heat exchangers substantially boosts heat transfer, with optimized fin designs notably improving both melting and solidification compared to using nanoparticles alone. Rogowski and Andrzejczyk [4] further emphasized the importance of geometric parameters, such as fin and coil configurations, showing that while numerical studies dominate the field, experimental validation — particularly at higher melting temperatures — is still insufficient.

Organic PCMs like coconut oil have also drawn attention due to their promising energy storage properties. Saleel [2] reviewed the heat transfer and melting behaviors of coconut oil PCMs, focusing on how nano-additives and metal foam inserts enhance the melting front, shorten phase change times, and increase heat transfer rates. In parallel, Low et al. [5] explored how different heat transfer interfaces — flat, extended, or direct contact — between the PCM and heat transfer fluid (HTF) significantly influence convective heat transfer coefficients, underscoring the importance of accessible and optimized interfaces for improving thermal performance.

Heat transfer enhancement in enclosures using fins and porous media has become a focal point of research due to its importance in enhancing the performance of energy systems, electronics cooling, and PCM storage units. Fins, by increasing the surface area and guiding convective currents, and porous media, by enhancing thermal conductivity and fluid mixing, both play vital roles in improving heat dissipation. Le et al. [6] numerically studied solid fins in a cubical enclosure with differential heating, showing that appropriate fin location and length can significantly intensify heat transfer. Specifically, fins placed near the cavity's bottom provided better performance, and excessive fin length beyond a certain point could actually reduce the average Nusselt number.

* Corresponding author.
E-mail addresses: j.jana@psau.edu.sa (J. Shafi), o.elamin@psau.edu.sa (O. Younis), stiari@widener.edu (S. Tiari), m.ghalambaz@gmail.com (M. Ghalambaz).

https://doi.org/10.1016/j.applthermaleng.2025.127960
Received 30 June 2025; Received in revised form 29 July 2025; Accepted 18 August 2025
Available online 19 August 2025

Improving heat transmission in latent heat TES (LHTES) enclosures employing fins and metal foams has become a major research focus to address the poor values of PCMs' thermal conductivity and improve their energy-storing performance [7]. Fins are a well-established method for extending the heat transmission surface area and guiding thermal gradients within LHTES systems [8]. A review by [9] highlighted that various fin shapes, including rectangular, annular, and spiral fins, can enhance heat transfer, with longitudinal rectangular fins offering excellent performance and ease of manufacture. Recent innovations, such as angled fins, have shown promise as well; [10] found that downward-angled fins at 10° reduced melting time by over 55 % and improved temperature uniformity by 20 %, demonstrating the importance of geometric fin optimization. Additionally, petal-shaped fins have been proposed to enhance PCM solidification. According to [11], an optimal rectangular part offset in the petal-shaped fin reduced solidification time by 23.6 % and tuning the volume ratio between the annular and rectangular parts further boosted performance. In [12], the fins have been used to improve the heat transfer in non-Newtonian PCMs.

Beyond fins, metal foams have attracted considerable attention due to their interconnected porous networks and high thermal conductivity, which help overcome the inherent low conductivity of PCMs. A comprehensive review by [13] summarized the state-of-the-art on PCM-metal foam composites, noting that foam pore size, porosity, and distribution critically influence thermal performance. Numerical studies, such as [14], revealed that the addition of metal foam significantly increases thermal dissipation compared to nano additives alone, especially when the foam spans the full height of the enclosure. Furthermore, functionally graded metal foams, as explored by [15], provide additional benefits by tailoring porosity across the enclosure, optimizing convection and melting behaviors. This strategy achieved up to a 15.8 % increase in average power density compared to uniform foams.

Anisotropic metal foams also offer novel enhancement pathways. [16] showed that placing anisotropic foam layers in the middle of the enclosure with a 0° orientation angle led to a 3.7 and a 2.3 % drop in melting and solidification time, respectively. This provides the importance of directional thermal pathways. Together, these studies [9–11,13–16] highlight how combining advanced fin designs with tailored metal foam structures holds substantial potential to improve heat transfer, reduce charging/discharging times, and maximize the efficiency of modern LHTES systems.

The shape and configuration of tubes in LHTES units play a critical role in determining the system's heat transfer efficiency and energy storage rate. Recent studies highlight that optimizing tube geometry can significantly enhance both melting and solidification performance by improving temperature distribution and convective flow within PCMs. Incorporating polygonal tubes in LHTES systems has shown substantial performance benefits over traditional circular tubes. For instance, one study demonstrated that polygonal tubes increased average heat flux by up to 14.53 % and thermal power by 21.21 %, while simultaneously reducing thermal entropy generation by 23.97 % compared to circular designs [17]. These improvements are attributed to the increased surface area and better flow dynamics offered by non-circular geometries.

Similarly, bionic-inspired designs, such as lotus root- and horsetail stem-shaped tubes, have proven effective in addressing melting dead zones and enhancing energy utilization. A lotus root-inspired multi-tube design reduced melting time by 89.1 % and improved effective power density by 7.6 times compared to a conventional single-tube unit [18]. Horsetail stem fin configurations further reduced melting and solidification times by 44.3 and 54.6 %, respectively, contributing to faster thermal response and better PCM utilization [19]. Furthermore, triangle-tube arrangements in multi-tube LHTES units with metal foam-enhanced PCMs reduced charging time by up to 10.4 %, while square-tube configurations performed better during discharge, reducing time by up to 27.8 % [20]. Thus, as seen, the tube shape and layout could notably influence the energy storage rate and should be carefully tailored to optimize specific charge/discharge phases.

Tube bundles and petal tubes have been shown to be excellent methods for enhancing heat transmission in LHTES enclosures. Numerical studies have shown that modifying tube-bundle arrangements can significantly enhance PCM melting and solidification performance by increasing the heat transmission area and optimizing fluid circulation. For example, [21] demonstrated that a modified tube-bundle design, which places half-cylindrical tubes in direct contact with the PCM, reduced melting and solidification times by up to 50 % compared to conventional double-pipe systems. Similarly, [22] showed that the placement of tube bundles within the enclosure directly affects natural convection patterns, with optimal arrangements achieving up to a 28 % increase in melting rates and a 94 % melting fraction after 4 h.

Petal-shaped tubes offer another enhancement route. Studies such as [11] and [23] found that petal tubes improve heat transfer uniformity and significantly reduce solidification and melting times compared to traditional annular or rectangular fins. Optimal petal designs, combined with nano-additives, achieved up to 45 % improvement in heat transfer over circular tubes [23], making them a promising avenue for high-efficiency LHTES systems.

The existing literature indicates that incorporating metal foams represents an effective strategy for enhancing heat transmission during both the melting and solidification phases of PCMs. However, the practical application of metal foams, frequently fabricated from high-value materials such as copper, often results in substantial increases in both the system's overall weight and its manufacturing cost. As an alternative, modifications to the geometric configuration of tubes and the optimization of tube bundle arrangements offer methods to influence the phase transition process. These approaches are particularly advantageous as they incur minimal additional weight and significantly lower material expenditures. Consequently, the present investigation endeavors to comprehensively examine, for the first time, the synergistic effect of petal-shaped tube bundles on the melting and solidification heat transmission performance of PCMs when these are integrated within metal foams. This novel approach seeks to advance thermal efficiency using a combination of metal foams and geometric improvements.

2. Physical model

2.1. Model description

the LHTES systems are highly effective technologies designed to harness solar energy and convert it into thermal energy for later use. Their key benefits include compact size, cost-effectiveness, and eco-friendly nature, making them well-suited for sustainable construction applications. Furthermore, these units enhance the durability of energy storage solutions, eliminate reliance on expensive chemical battery storage, and significantly contribute to broader adoption of renewable energy systems.

A practical implementation of LHTES within solar energy applications is shown in Fig. 1. In this configuration, solar collectors absorb sunlight, converting it into thermal energy that heats water passing through the collector. A pump subsequently transfers this heated water to a storage tank, incrementally increasing its internal temperature. Additionally, a secondary pumping mechanism transfers water between the storage tank and the LHTES unit, thus effectively storing thermal energy within the LHTES unit. The heated water stored in the tank becomes available to meet building demands for hot water.

When solar radiation is limited or the demand for hot water exceeds typical levels, the storage tank water temperature may decrease below the specific phase-change temperature of the LHTES unit. Consequently, the thermal energy previously stored in the LHTES is discharged back into the water tank, maintaining a consistent and reliable hot water temperature. This ensures a constant supply of hot water regardless of variable solar conditions or increased consumption requirements.

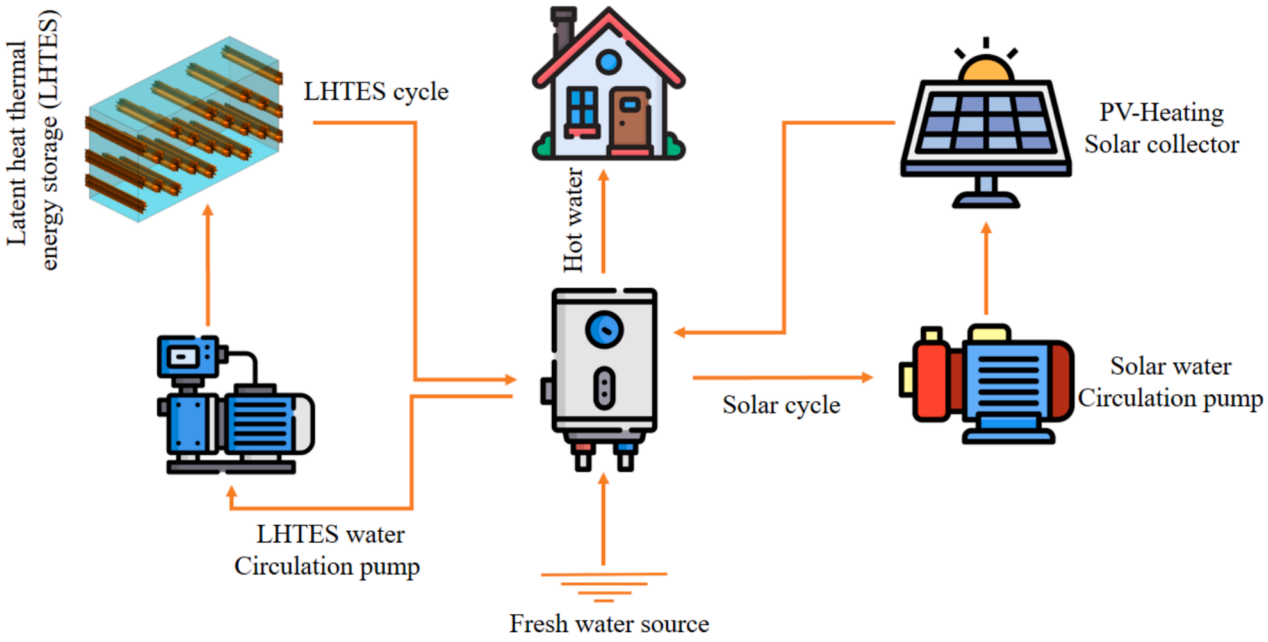

Fig. 1. The schematic view of the TES cycle.

While LHTES units are capable of storing significant amounts of thermal energy, their low thermal performance limits their effectiveness in energy systems. Therefore, techniques to enhance heat transfer are necessary to improve their performance. Petal tubes offer an extended surface area, which directly improves heat transmission within the PCM domain. Additionally, metal foams provide a structure that further improves heat transfer in the PCM domain. Metal foams offer excellent thermal performance for LHTES but face scalability challenges due to high fabrication costs, especially with powder metallurgy. However, methods like melt gas injection using recycled metals can reduce

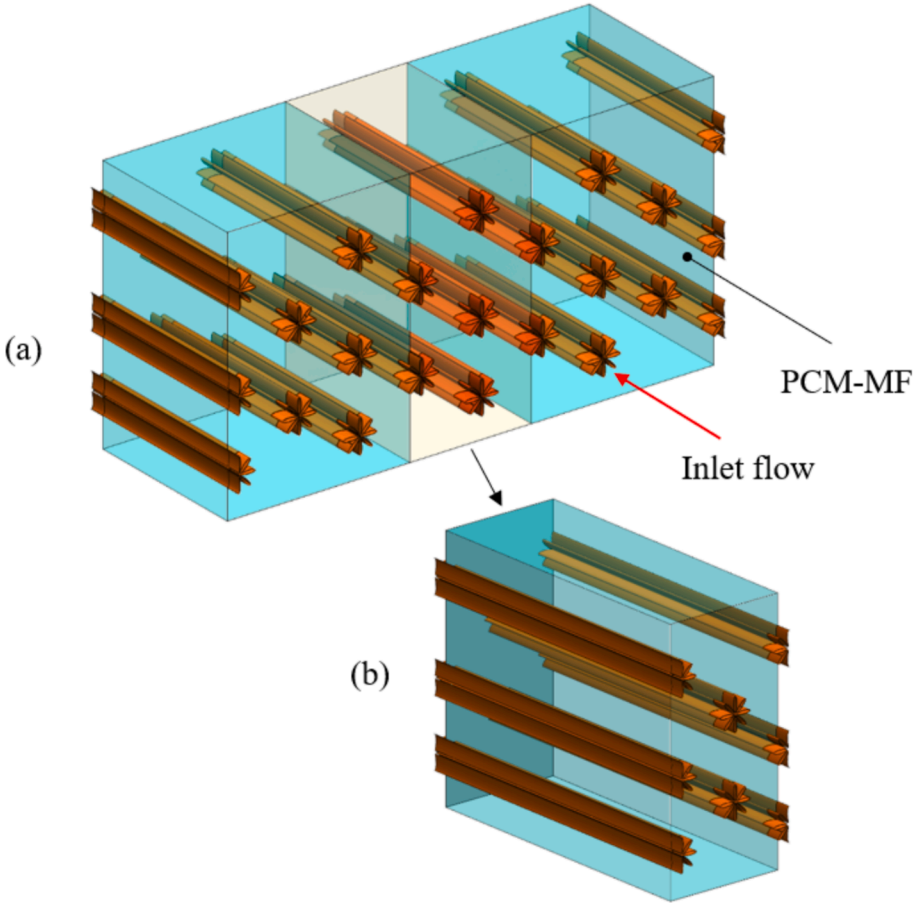

Fig. 2. The energy storage unit and petal tube bundle. (a) The full domain, and (b) a periodic section of domain for physical modeling.

expenses. Advances in additive manufacturing and cheaper blowing agents may further lower costs, improving the feasibility of metal foams for larger-scale thermal storage applications [24]. Therefore, using less metal foam by partial metal foam filling [25] or approaches that enhance heat transfer rates, such as the optimal placement of petal-shaped tubes in combination with metal foams—remain of significant interest. The objective of the current research is to assess the impact of petal-shaped tubes and metal foams on the thermal performance of an LHTES unit.

It is worth noting that some versions of semi-circular petal-shaped tubes have been manufactured and are available [26]. The aim of the present study is to analyze the potential thermal advantages of using petal tubes in metal foam–PCM composite applications, assuming perfect thermal contact between the metal foam and the petal tubes. However, inserting such petal tubes into metal foams and achieving a perfect contact surface between the tube and the foam poses a manufacturing challenge, which should be addressed during the production process and is beyond the scope of the present study.

A bundle of petal-shaped tubes is utilized through which the HTF flows. A schematic representation of this bundle is shown in Fig. 2(a). The space between the tubes is loaded with the PCM, which is embedded within open metal foams. During the charging process, the hot HTF passes through the petal tubes and transfers heat to the surrounding PCM via conduction, leading to the melting of the PCM. As the PCM melts into a liquid state, natural convection effects within the PCM domain intensify, initiating natural convection flow. The molten PCM is able to move through the open cells of the metal foam, enhancing the heat transfer process. The melting region around one tube can influence the melting process surrounding adjacent tubes, leading to a larger-scale melting phenomenon.

In the energy release process, the cold fluid flows through the petal tubes and begins to freeze the molten PCM surrounding the tubes. As some liquid PCM remains hot, natural convection effects are again observed, with downward convection flows expected in the molten region. The tube bundle geometry is repeated in the direction perpendicular to the tubes. A periodic section of the model is depicted in Fig. 2 (b), where, by assuming long tubes, boundary effects are neglected. For high HTF flow rates, a constant temperature on the inner wall of the tubes can be assumed. With these assumptions, the thermal energy storage in the bundle is modeled as shown in Fig. 3. The geometrical arrangement of the model is displayed in Fig. 3(a), while the boundary conditions are shown in Fig. 3(b). A detailed view of a petal-shaped tube is presented in Fig. 3(c). The petal tubes can be positioned at different vertical locations to maximize the natural convection effects when there is a substantial amount of liquid PCM in storage. The placement of the left and right tubes is governed by three geometric parameters, namely HL_0, HL_1, and HL_2. The middle tubes are similarly controlled by these parameters. A periodic boundary condition is applied to the flow and heat transmission at the left and right edges of the domain.

The petal geometry is introduced by a polygon using x and y coordinates introduced as [27]

$$\begin{cases} x = (r_c + \lambda \sin(N \times S))\cos(S) \\ y = (r_c + \lambda \sin(N \times S))\sin(S) \end{cases} \quad (1)$$

where $S = \{0,\ 0.03,\ 0.06,\ \ldots,\ 2\pi\}$. The area of petals remained constant as the number and amplitude of petals changed. Thus, the amount of PCM in all cases is the same. Besides, the geometrical configuration is as follows. A module height $H_b = 11D$, a module width $H_L = 3\sqrt{3}D$, $D = 28.6$ mm, where D is the characteristics parameter of the study and is equal to the diameter of a circle tube with the same area as the petals. The petal area is computed as $A_p = \pi D^2/4$, and $r_c = \sqrt{A_p/\pi - \lambda^2}/2$ [23]. An axillary characteristics length is also defined as $H = 11D/3$, which was used for scaling the location of tubes.

2.2. Mathematical model

The governing equations that describe the heat transfer phenomena

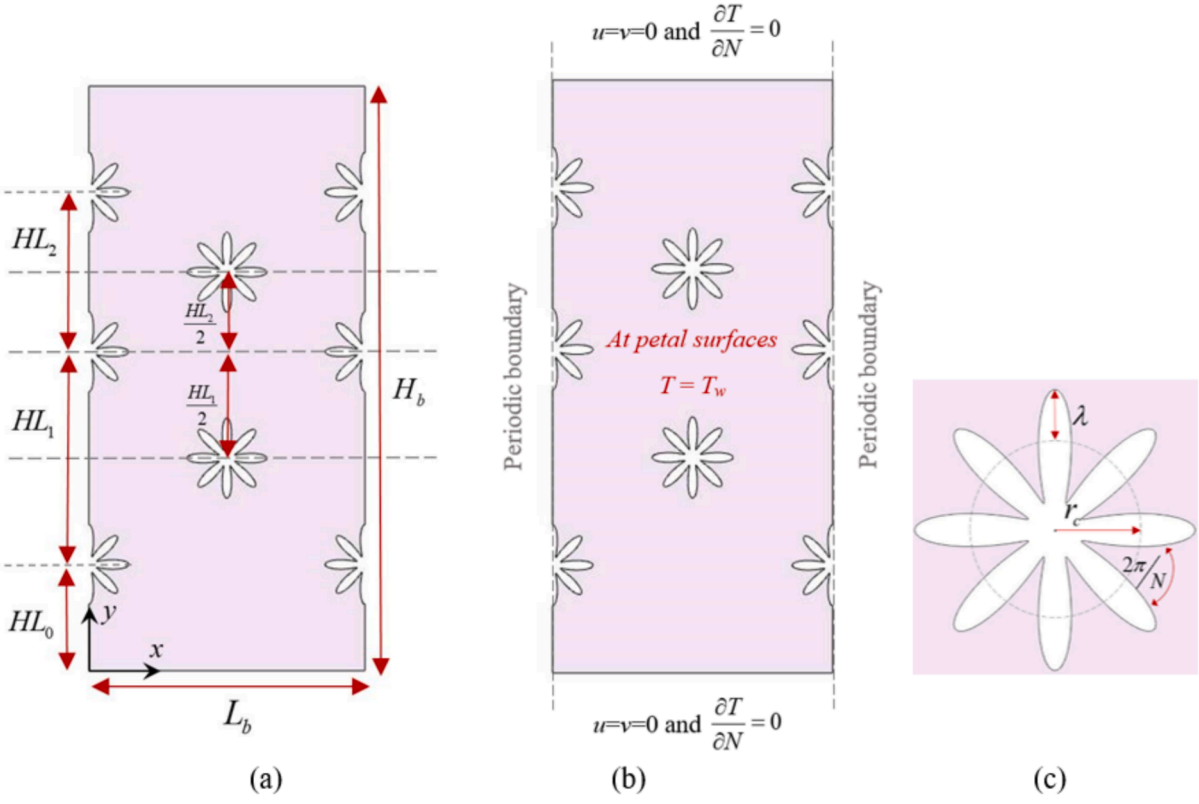

Fig. 3. The model details. (a) geometrical definition of the physical domain, (b) the applied boundary conditions, and (c) a detailed view of a petal.

within a composite domain of PCM and metal foam are expressed through partial differential equations. The Local Thermal Non-Equilibrium (LTNE) approach is utilized to distinctly model the heat conduction mechanisms occurring separately in the PCM and the metal foam [28,29]. The LTNE effects are important at early times of phase change [30]. Source terms are integrated into the equations to reflect energy interaction between these distinct phases.

Within the molten PCM occupying the open-cell structure of the metal foam, natural convection flow is considered significant. Hence, the continuity and momentum equations are rigorously applied to this composite PCM-metal foam domain. The enthalpy-porosity technique is employed to effectively simulate the PCM phase change process, with momentum source terms included to constrain velocities within solid PCM regions by relating them to the liquid fraction (f).

To accurately represent fluid flow behavior within the porous structure of the metal foam, the Darcy-Brinkman-Forchheimer model is implemented. Due to relatively limited temperature variations (~30°) observed during the analysis, most physical properties were assumed constant, except for those associated with the PCM, which exhibit changes during the melting process. Additionally, to incorporate the buoyancy-driven flow arising from thermal gradients in the liquid PCM, the Boussinesq approximation is applied. Given the limited temperature ranges examined, most thermophysical properties remained constant, with the notable exception of the PCM properties during its phase transition period. The conservation of mass, momentum, and energy equations underpinning this analysis are presented in partial differential form, referencing previous literature [31–33]:

Continuity:

$$\left(\frac{\partial u}{\partial x}+\frac{\partial v}{\partial y}\right)=0 \tag{2}$$

Momentum:

$$\frac{\rho_{\mathrm{PCM}}}{\varepsilon}\frac{\partial u}{\partial t}+\frac{\rho_{\mathrm{PCM}}}{\varepsilon^2}\left(u\frac{\partial u}{\partial x}+v\frac{\partial u}{\partial y}\right)=-\left(\frac{\partial p}{\partial x}\right)+\frac{1}{\varepsilon}\left[\frac{\partial}{\partial x}\left(\mu_{\mathrm{PCM}}\frac{\partial u}{\partial x}\right)+\frac{\partial}{\partial y}\left(\mu_{\mathrm{PCM}}\frac{\partial u}{\partial y}\right)\right] -\frac{\mu_{\mathrm{PCM}}}{\kappa}u-\rho_{\mathrm{PCM}}\frac{C_F}{\sqrt{\kappa}}|U|u-A_{mush}\frac{(1-f(T))^2}{\lambda_{mush}+f^3(T)}u \tag{3a}$$

$$\frac{\rho_{\mathrm{PCM}}}{\varepsilon}\frac{\partial v}{\partial t}+\frac{\rho_{\mathrm{PCM}}}{\varepsilon^2}\left(u\frac{\partial v}{\partial x}+v\frac{\partial v}{\partial y}\right)=-\left(\frac{\partial p}{\partial y}\right)+\frac{1}{\varepsilon}\left[\frac{\partial}{\partial x}\left(\mu_{\mathrm{PCM}}\frac{\partial v}{\partial x}\right)+\frac{\partial}{\partial y}\left(\mu_{\mathrm{PCM}}\frac{\partial v}{\partial y}\right)\right] +g\rho_{\mathrm{PCM}}\beta_{\mathrm{PCM}}(T-T_0)-\frac{\mu_{\mathrm{PCM}}}{\kappa}v-\rho_{\mathrm{PCM}}\frac{C_F}{\sqrt{\kappa}}|U|v-A_{mush}\frac{(1-f(T))^2}{\lambda_{mush}+f^3(T)}v \tag{3b}$$

Conservation of energy in the PCM:

$$\varepsilon(\rho C_p)_{\mathrm{PCM}}\frac{\partial T_{\mathrm{PCM}}}{\partial t}+(\rho C_p)_{\mathrm{PCM}}\left(u\frac{\partial T_{\mathrm{PCM}}}{\partial x}+v\frac{\partial T_{\mathrm{PCM}}}{\partial y}\right)= \frac{\partial}{\partial x}\left(k_{\mathrm{eff,PCM}}\frac{\partial T_{\mathrm{PCM}}}{\partial x}\right)+\frac{\partial}{\partial y}\left(k_{\mathrm{eff,PCM}}\frac{\partial T_{\mathrm{PCM}}}{\partial y}\right)+h_v(T_{\mathrm{MF}}-T_{\mathrm{PCM}})-\varepsilon\rho_{\mathrm{PCM}}L_{\mathrm{PCM}}\frac{\partial f(T)}{\partial t} \tag{4a}$$

Conservation of energy in the metal foam:

$$(1-\varepsilon)(\rho C_p)_{\mathrm{MF}}\frac{\partial T_{\mathrm{MF}}}{\partial t}=\frac{\partial}{\partial x}\left(k_{\mathrm{eff,MF}}\frac{\partial T_{\mathrm{MF}}}{\partial x}\right)+\frac{\partial}{\partial y}\left(k_{\mathrm{eff,MF}}\frac{\partial T_{\mathrm{MF}}}{\partial y}\right)-h_v(T_{\mathrm{MF}}-T_{\mathrm{PCM}}) \tag{4b}$$

The previously discussed equations incorporate fundamental parameters including gravitational acceleration (g), volumetric thermal expansion coefficient (β), latent heat of fusion (L), metal foam permeability (κ), and the Forchheimer coefficient (C_F). Additionally, the model integrates interstitial volumetric convective heat transfer (h_v), determined using the Nusselt number at the pore-scale [34]. Specific subscripts such as PCM for phase change material, MF for metal foam, and eff for effective combined properties are introduced to clarify various material characteristics. To ensure that fluid velocities are effectively zero within the solid PCM regions, the model incorporates specialized source terms, A_{mush} and λ_{mush}. A_{mush} is set at a substantially large magnitude (1E10 Pa·s/m^2) to dominate the flow equations and suppress fluid flow in the solid PCM areas [16,28]. Conversely, λ_{mush} is assigned a minimal value of 0.001, serving to prevent numerical instabilities from division by zero scenarios. The presence of metal foam introduces significant flow resistance to the liquid PCM. Therefore, the values of the momentum sink term coefficient (A_{mush}) must be sufficiently large to generate artificial damping forces that dominate over the natural resistance of the porous medium. As a result, the fluid velocity approaches zero within the solid regions, effectively mimicking the behavior of a solid phase.

Moreover, solver stability and enforced stationary conditions within the solid PCM areas are achieved through implementing a viscosity model that dynamically depends on the liquid fraction (f). The mathematical formulation is presented as $\mu = A_\mu(1–f) + \mu_{\mathrm{PCM,l}} \times f$, with A_μ denoting a significantly high viscosity constant (10^4 Pa·s). Under this model, when f is close to one, viscosity aligns closely with the typical liquid-phase viscosity ($\mu_{\mathrm{PCM,l}}$). In contrast, when f nears zero, viscosity escalates substantially, reflecting the significant resistance to fluid flow characteristic of the solid state. Besides, $|U|$ is the velocity magnitude and is defined as $|U|=(u^2+v^2)^{1/2}$.

The thermal transport equations for the PCM and metal foam phases under the Local Thermal Non-Equilibrium (LTNE) assumption are outlined explicitly in Eqs. (4a) and (4b), respectively. Interaction between these two phases is depicted through the coupling term $h_v(T_M– T_{\mathrm{PCM}})$, accounting for convective thermal exchange at their interface. Effective thermal conductivities $k_{\mathrm{eff,PCM}}$ and $k_{\mathrm{eff,MF}}$ are employed to represent the impact of the porous structure on thermal conductivity [35]. The temperature-dependent liquid volume fraction (f) follows a functional relationship as [36]:

$$f(T)=\begin{cases}0 & T<-\frac{1}{2}\Delta T_{\mathrm{f}}+T_{\mathrm{f}}\ (\mathrm{Solid})\\ \frac{1}{2}+\frac{(T-T_{\mathrm{f}})}{\Delta T_{\mathrm{f}}} & -\frac{1}{2}\Delta T_{\mathrm{f}}+T_{\mathrm{f}}\le T\le\frac{1}{2}\Delta T_{\mathrm{f}}+T_{\mathrm{f}}\ (\mathrm{Mixture})\\ 1 & T>\frac{1}{2}\Delta T_{\mathrm{f}}+T_{\mathrm{f}}\ (\mathrm{Liquid})\end{cases} \tag{5}$$

Building upon previous studies [31,35,37], the metal foam's effective thermal conductivity (k_{a}) and the average permeability (κ_{a}) are calculated as follows:

$$k_a=\left(\frac{1-\varepsilon}{3}\right)k_{\mathrm{MF}} \tag{6a}$$

$$\kappa_a=\frac{\varepsilon^2}{36}\frac{\left(d_{fp}\sqrt{\frac{\kappa_{tor}}{3\varepsilon}}\right)^2}{\kappa_{tor}(\kappa_{tor}-1)} \tag{6b}$$

Further equations need to be incorporated that involve d_{fs} and λ_{tor}. These formulations describe the bulk thermal conductivity k_{MF} of the metal foam material and can be detailed as indicated in [37]:

$$d_{fs}=1.18\sqrt{\frac{1-\varepsilon}{3\pi}}\left\{\frac{1}{1-e^{\frac{(\varepsilon-1)}{0.04}}}\right\}d_{fp} \tag{7c}$$

$$\frac{1}{\kappa_{tor}}=\frac{3}{4\varepsilon}+\frac{\sqrt{9-8\varepsilon}}{2\varepsilon}\cos\left\{\frac{4\pi}{3}+\frac{1}{3}\cos^{-1}\left(\frac{8\varepsilon^2-36\varepsilon+27}{(9-8\varepsilon)^{\frac{3}{2}}}\right)\right\} \tag{7d}$$

Here d_{fp} based on pore per inch and C_F were assessed as described in [37]:

$$d_{fp} = \frac{0.0254}{PPI} \tag{7e}$$

$$C_F = 0.00212(1-\varepsilon)^{-0.132}\left(\frac{d_{fs}}{d_{fp}}\right)^{-1.63} \tag{7f}$$

The interstitial volumetric heat exchange factor was employed to assess the thermal interaction occurring between the PCM and the metal foam across the porous structure, particularly under flow conditions characterized by minimal Reynolds numbers, as described in prior scholarly analyses. [34]:

$$h_v = Nu_v \frac{k_{\mathrm{PCM}}}{d_{fs}^2} \tag{8a}$$

$$Nu_v = \begin{cases} 76.99 - 152.01\varepsilon + 75.04\varepsilon^2 & 0 \le \mathrm{Re} \le 0.1 \\ (1.72 + 1.71\varepsilon - 3.46\varepsilon^2)\mathrm{Re}^{0.26}Pr^{0.28} & 0.1 < \mathrm{Re} \le 1 \end{cases} \tag{8b}$$

In the set of equations described earlier, the parameters Re, Pr, and α symbolize, respectively, the Reynolds number, Prandtl number, and thermal diffusivity at the pore level. Here, the Reynolds number is determined using the density, velocity, and characteristic diameter associated with the solid regions of the PCM. The Prandtl number, expressed as $\mathrm{Pr} = \mu\rho/\alpha$, incorporates the dynamic viscosity (μ), density (ρ), and thermal diffusivity (α) of the PCM. Thermal diffusivity itself is calculated by the formula $\alpha = k / (C_p\ \rho)$, where k refers to thermal conductivity and C_p represents specific heat capacity.

Although numerous formulas for estimating the Nusselt number can be found in existing research, most are valid only when the Reynolds number is greater than one. Given that, in this investigation, the PCM's circulation speed inside the metal foam typically results in Reynolds numbers below unity, the study adopts a correlation proposed by Yao et al. [34], specifically formulated for low-Reynolds-number conditions. This empirically derived relation has been confirmed through experiments and aligns closely with the thermal behavior of PCM undergoing phase transformation within MF structures. Additionally, the PCM's effective thermal conductivity is determined using the equation provided in prior works [31,35]. It is worth noting that Eq. (8) is accurate when $21 < \mathrm{Pr} < 41$ and $0.929 < \varepsilon < 0.974$.

$$k_{\mathrm{eff,\ PCM}} = \frac{2+\varepsilon}{3} k_{\mathrm{PCM}} \tag{9}$$

As shown by the equations below, the thermophysical characteristics of the PCM were calculated using a mean of phases as:

$$(\rho C_p)_{\mathrm{PCM}} = f(\rho C_p)_s + (1-f)(\rho C_p)_l \tag{10a}$$

$$\rho_{\mathrm{PCM}} = f\rho_s + (1-f)\rho_l \tag{10b}$$

Within this context, the solid (s) and liquid (l) PCM phases are denoted by s and l subscripts, respectively. Table 1 provides a summary outlining the thermophysical characteristics of the copper (metal foam and tube), and paraffin (PCM).

The PCM's melting temperature interval, spanning 49 to 54 °C, along with its fusion latent heat of $L = 1.76\mathrm{E}5$ J/kg [39]. The PCM's dynamic viscosity (3.6E-3 kg/m·s) and its coefficient of thermal expansion (0.0009 1/K) [39–41] were used.

Table 1
Material Properties of copper and paraffin.

Materials	ρ (kg/m^3)	k (W/m.K)	C_p (J/kg.K)
Copper [38]	8900	380	386
Paraffin (solid/liquid) [39–41]	916/790	0.21/0.12	2700/2900

2.3. The boundaries and initial conditions

During the melting process, the heated wall was set to a high temperature of $T_{wall} = T_f + 15$ °C. The starting temperature of the system was set at $T_0 = T_f - 15$ °C. During the solidification process, $T_{wall} = T_f - 15$ °C, and the starting temperature of the system was set at $T_0 = T_f + 15$ °C. A reference temperature of $T_{ref} = T_f - 15$ °C was used to define a relative temperature of $\Delta T = T\text{-}T_{ref}$ for the graphical presentation of the results. All other walls were treated as insulated, with no heat flow allowed ($-\mathrm{n}\cdot q = 0$).

Every wall surface followed no-slip and impermeable boundary conditions. A point with zero relative pressure was placed at the lower left corner of the container. The periodic boundary condition was applied to the periodic surfaces. For the periodic flow, the velocity and pressure at the source and destination were matched as follows:

$$u_{src} = u_{dst},\ v_{src} = v_{dst} \tag{11a}$$

$$p_{src} = p_{dst} \tag{11b}$$

Where subscripts of *src* and *dst* indicate the source and distention periodic boundaries. For the heat equation, the heat flux and temperatures were matched in the MF and PCM as follows:

$$-n_{src,MF}\cdot q_{src,\ MF} = n_{dst} q_{dst,MF},\ T_{src\ ,MF} = T_{dst,\ MF} \tag{12a}$$

$$-n_{src,PCM}\cdot q_{src,\ PCM} = n_{dst} q_{dst,PCM},\ T_{src\ ,PCM} = T_{dst,\ PCM} \tag{12b}$$

where the negative sign for the *src* side accounts for the change of surface direction.

2.4. Parameters of interest

The quantity of molten PCM is described by the melting volume fraction, which was calculated by integration over domain of solution as:

$$MVF = \frac{\oint_V \varepsilon f dV}{\oint_V \varepsilon dV} \tag{13a}$$

In this equation, dV represents the volumetric element within the shell domain with in a unit depth. The total thermal energy stored in the system is the sum of both latent and sensible heat, which can be calculated using the equations:

$$Q_{sensible} = \left[\oint_V \left(\int_{T_0}^{T} \varepsilon(\rho C_P)_{\mathrm{PCM}}(T)dT\right)dV\right] + (T-T_0)(\rho C_P)_{\mathrm{MF}}\oint_V (1-\varepsilon)dV \tag{13b}$$

$$Q_{latent} = \varepsilon \oint_V \rho_{\mathrm{PCM}} f L_{\mathrm{PCM}} dV \tag{13c}$$

The overall stored energy, Q_{store}, is the sum of sensible and latent heat contributions:

$$Q_{store} = Q_{sensible} + Q_{latent} \tag{13d}$$

3. Numerical strategy and simulation verification

This part provides an overview of the numerical route adopted, the evaluation of mesh refinement effects, and the procedures used to test the model's dependability.

3.1. Use of finite element framework

The foundational equations, along with their corresponding starting values and edge settings, were tackled using the finite element framework (FEM). This computational scheme was selected for its strength in

dealing with complex source/sink components caused by the melting and solidifying process, as referenced in [42,43].

Instead of using the strong form, the equations were expressed in a weak formulation. The energy and fluid flow equations were broken into second-order discrete forms. By applying Gauss quadrature at the element level, a group of algebraic residual equations was obtained. These residuals were solved through a coupled and repeated method, employing the Newton-Raphson technique [44,45], which was stabilized by a damping factor of 0.9 to help with smoother convergence. To carry out a large number of calculations, the PARDISO parallel algorithm was integrated, taking advantage of multicore processing [46,47]. The progression of simulation time steps and the rate of solution refinement were dynamically managed, ensuring that the difference between solution updates stayed below a relative error of 10^{-4}. This was controlled using a backward difference method of either first or second order, depending on the need for numerical steadiness.

FEM was chosen for its ability to produce balanced and continuous results throughout a split domain, which matched the demands of this work. The simulations were initiated from default conditions and explored the charging and discharging behavior of thermal storage, including phase shift patterns. Both thermal transport and mass conservation equations, alongside the phase-tracking term (f), were

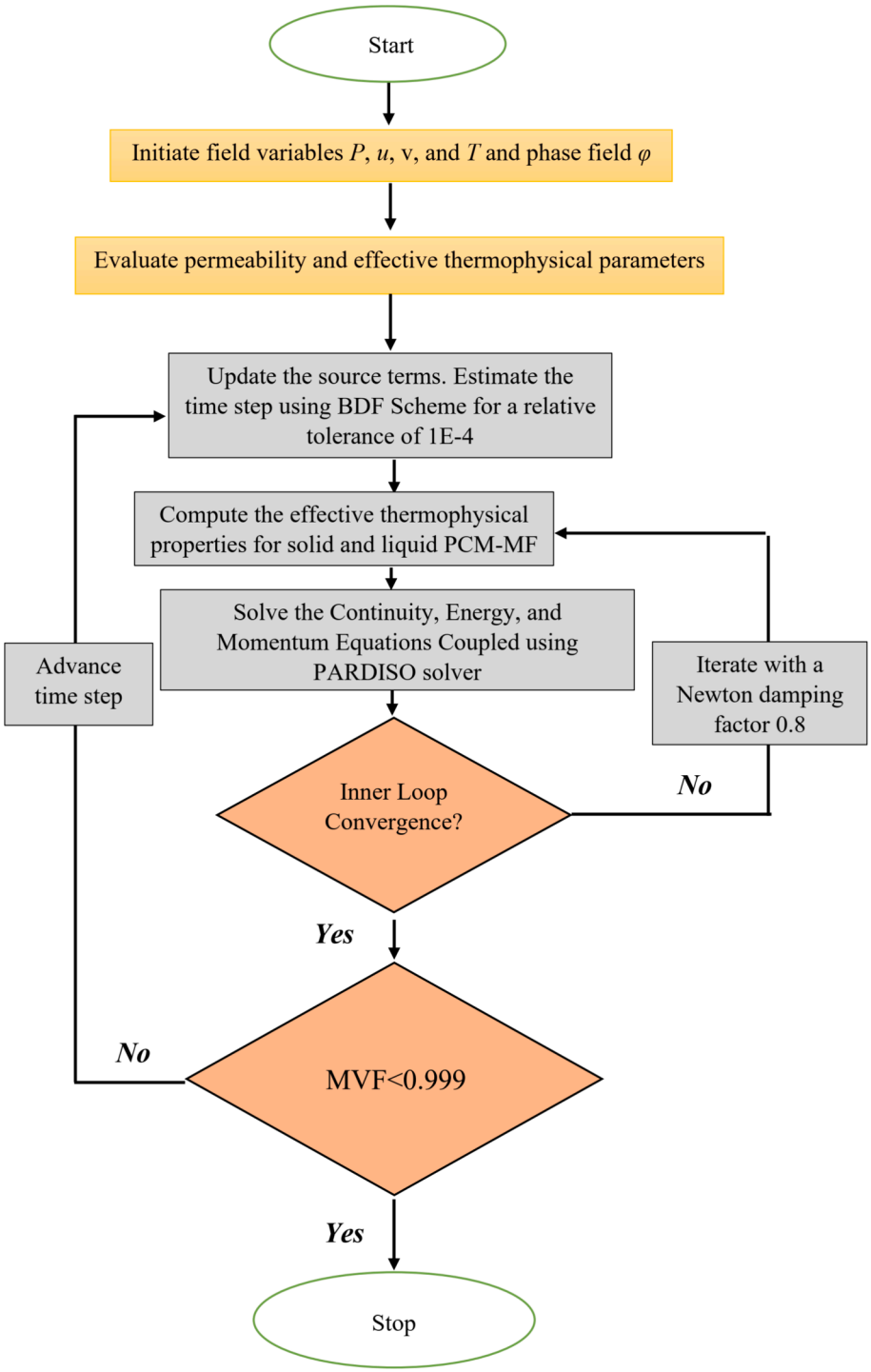

Fig. 4. The flowchart of an applied numerical method for simulation of phase change in LHTES.

incorporated directly into the solver and addressed in loops until a stable output was reached. The simulation was designed to stop when the phase transition had nearly concluded. For melting scenarios, the calculation ceased when the liquid fraction, MVF, was equal to or exceeded 0.99. In contrast, for freezing cases, an MVF below 0.01 was used as the end condition. The overall structure of the computational procedure is illustrated in Fig. 4.

3.2. Mesh sensitivity study

The influence of the grid dimensions on the precision of the numerical results was investigated using an example scenario with $N = 8$, $\lambda/r_c = 0.6$, $HL_0=H/2$, $HL_1=H$, and $HL_2=H$ where $H = 11D/3$ and $L=H$ were selected. The melting process was examined for different mesh sizes.

The domain of the solution was discretized using a structured mesh, with the mesh size controlled by a parameter called the mesh resolution, denoted as *Nm*. This parameter directly influences the number of elements in the mesh and, subsequently, the accuracy and computational time of the simulation. As the value of *Nm* increases, the mesh becomes finer, providing higher resolution and more accurate results. However, this comes at the cost of increased computational resources. Table 2 provides an overview of the mesh characteristics for different values of *Nm*, showing the number of edge elements, triangles, and total elements for each mesh. A non-uniform triangular mesh was used. Besides, the mesh elements were linked on the periodic boundaries, so they represent similar structures on the pair boundaries, which leads to better accuracy and solver stability.

The influence of different mesh sizes on the results was evaluated by analyzing the MVF throughout the melting process. The MVF curves for different mesh sizes were plotted in Fig. 5, and it was observed that the results for different mesh sizes closely aligned with one another. As the mesh resolution increased, the results converged, indicating that finer meshes produced only marginal improvements in accuracy. In particular, the curves for mesh sizes of $Nm = 2.0$, $Nm = 2.25$, and higher values were nearly identical, suggesting that further mesh refinement beyond this point provided little additional benefit. After considering both the accuracy and the computational time, a mesh resolution of $Nm = 2.25$ was selected for the simulations. This mesh size provided a good balance between accuracy and computational efficiency. Since the results for $Nm = 2.25$ were virtually indistinguishable from those of higher resolution meshes, it was concluded that this mesh size offered optimal performance without unnecessarily increasing computational load.

Fig. 6 illustrates the selected mesh with a mesh regulation factor $Nm = 2.25$ at various critical locations, including the petal tips, petal edges, and domain boundaries. As shown, the mesh is denser around the petal edges, which helps to better capture the intricate curves of the petals. This refined mesh ensures that the geometric features of the petals are accurately represented in the simulation. In addition to the finer mesh around the petal edges, a fairly fine mesh was applied both at the edges and within the internal domain. This is particularly important because the phase change region, which is a key area of interest in the simulation, moves through the internal domain. To capture the dynamics of this phase transition with high accuracy, a higher resolution in this region is necessary. The fine mesh ensures that the details of the phase change are precisely resolved. Furthermore, the mesh at the domain boundaries is also finely resolved to effectively capture the field gradients. This is crucial for accurately modeling the heat transfer and momentum exchange near the boundaries, where rapid changes in the solution can occur.

Table 2
Grid details for different settings of the mesh regulation factor *Nm*.

Nm	Edge elements	Triangles	Total Elements
2.0	2913	75,995	75,995
2.25	**3020**	**86,578**	**86,578**
2.5	3125	97,985	97,985
2.75	3236	109,276	109,276

Selected Mesh Nm = 2.25.

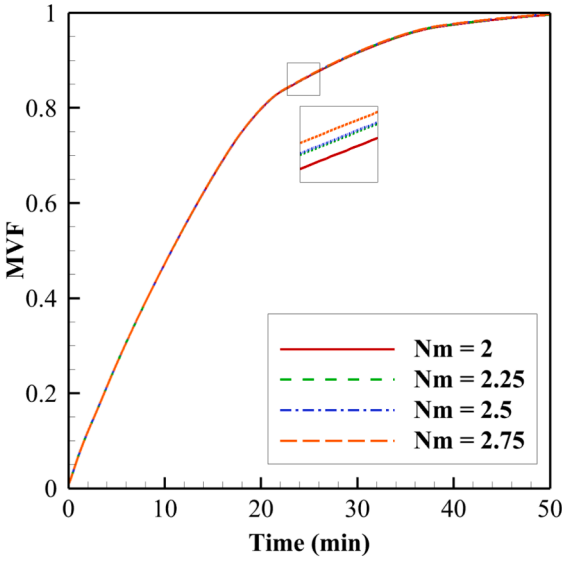

Fig. 5. The influence of mesh factor *Nm* on the time history of MVF throughout the melting process.

3.3. Model verification

Zheng et al. [38] experimentally investigated heat transfer during the melting of PCMs embedded in copper foam. Their setup captured key parameters such as solid–liquid interface evolution, temperature profiles, wall temperature variations, and total melting time. The apparatus included a data acquisition system, DC power supply, high-definition camera, and a polyurethane-insulated test section. A transparent acrylic sheet allowed direct observation, with insulation removable for imaging.

The PCM was placed in a rectangular polyethylene container, heated by a 100 × 10 × 30 mm^3 electrical heater supplying uniform heat flux. Eighteen T-type thermocouples (±0.1 °C) measured internal temperatures, heat loss, and ambient conditions. Temperature readings were taken every 10 s, and images captured every 30 min. Experiments were repeated for accuracy, with an overall uncertainty of ~ 7.04 %. The model assumed copper foam isotropy, laminar flow, and thermal equilibrium. Fig. 7 depicts a visual comparison of the observed melting interface and the simulated data. Fig. 8 presents the time evolution of the mean temperature at the heated wall, comparing experimental measurements with numerical simulation results. The maximum simulation-experiment temperature deviation was ~6 % at 120 min. Good agreement in melting interface and wall temperature profiles (Figs. 7–8) validated the numerical model.

4. Results section

In this research, the influence of the number of petals (N), petal amplitude (λ), and petal tube location configurations (HL_0, HL_1, and HL_2) on the phase change heat transmission and stored energy was investigated. A list of numerical experiment cases is listed in Table 3.

During the charging process, the MVF of the liquid phase begins at zero (MVF = 0), indicating a fully solid state, and gradually increases as the phase change progresses. A value of MVF = 1.0 signifies that the entire enclosure has transitioned to the molten phase. However, as the liquid fraction increases, the rate of charging typically declines, making it time-consuming and often impractical to achieve complete melting.

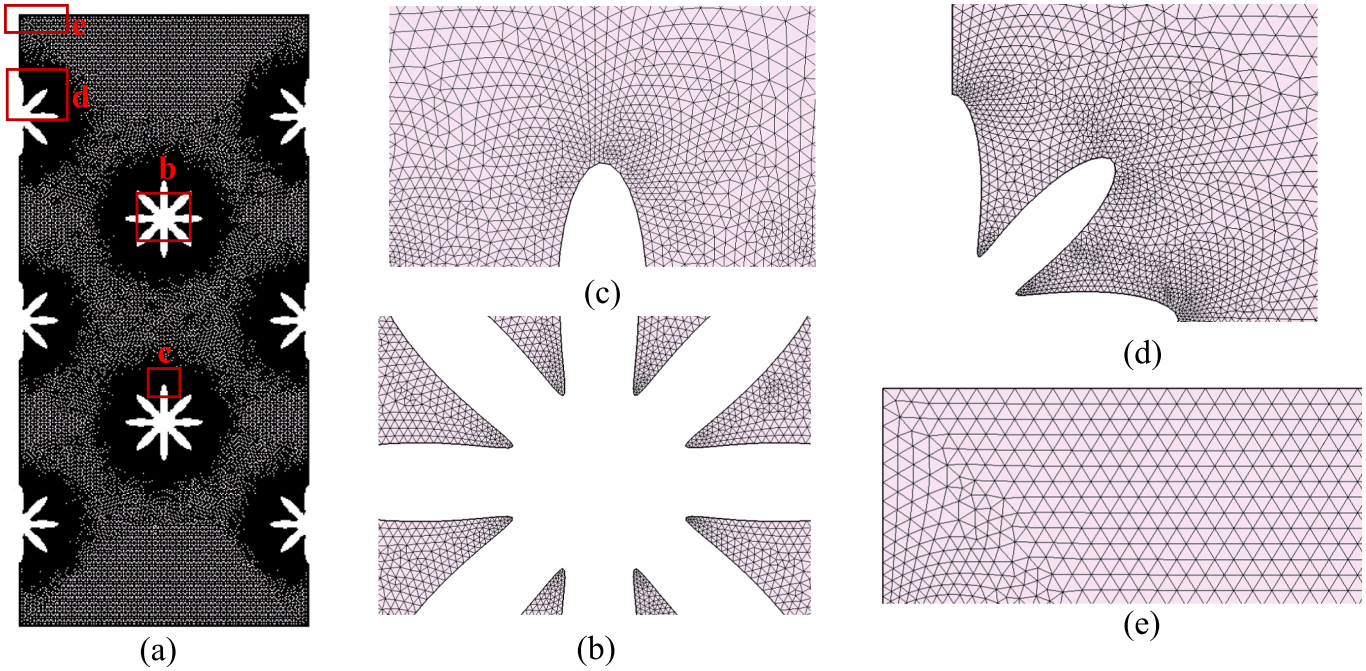

Fig. 6. A view of mesh for $Nm = 2.25$. This mesh was selected for computing the results.

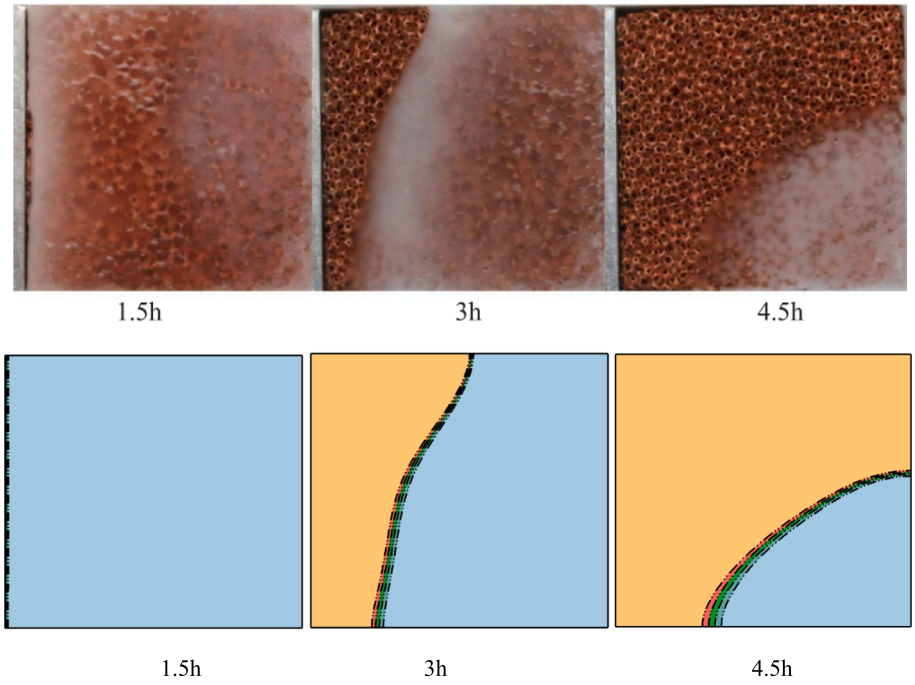

Fig. 7. Comparison of data with experiments of Zheng et al. [38].

Consequently, a state characterized by MVF = 0.9, corresponding to 90 % melting, is commonly adopted in the literature as a practical benchmark for evaluating the thermal performance of LHTES units.

Similarly, during the discharging process, the MVF decreases from an initial value of 1.0, representing a fully molten state. A fully discharged system corresponds to MVF = 0. An intermediate state, such as MVF = 0.1 (90 % discharge), serves as a practical and representative condition for analyzing the thermal behavior and determining the time required to reach near-complete solidification. These threshold values (MVF = 0.9 for charging and MVF = 0.1 for discharging) are well-established in previous studies and have been used as reference points for performance evaluation [48,49].

4.1. Petal number and amplitude

Fig. 9 illustrates the melting (Fig. 9a) and solidification (Fig. 9b) histories based on the melting volume fraction (MVF) for various petal numbers (N). Additionally, Fig. 10 presents contours of the liquid fraction (f) and temperature (ΔT) for selected cases: $N = 4$ (G1), $N = 8$ (G5), and a simple circular tube without petals, $N = 0$ (G15). When plotting the liquid fraction contours (f), the blue color indicates the solid region, while the red color represents the molten region.

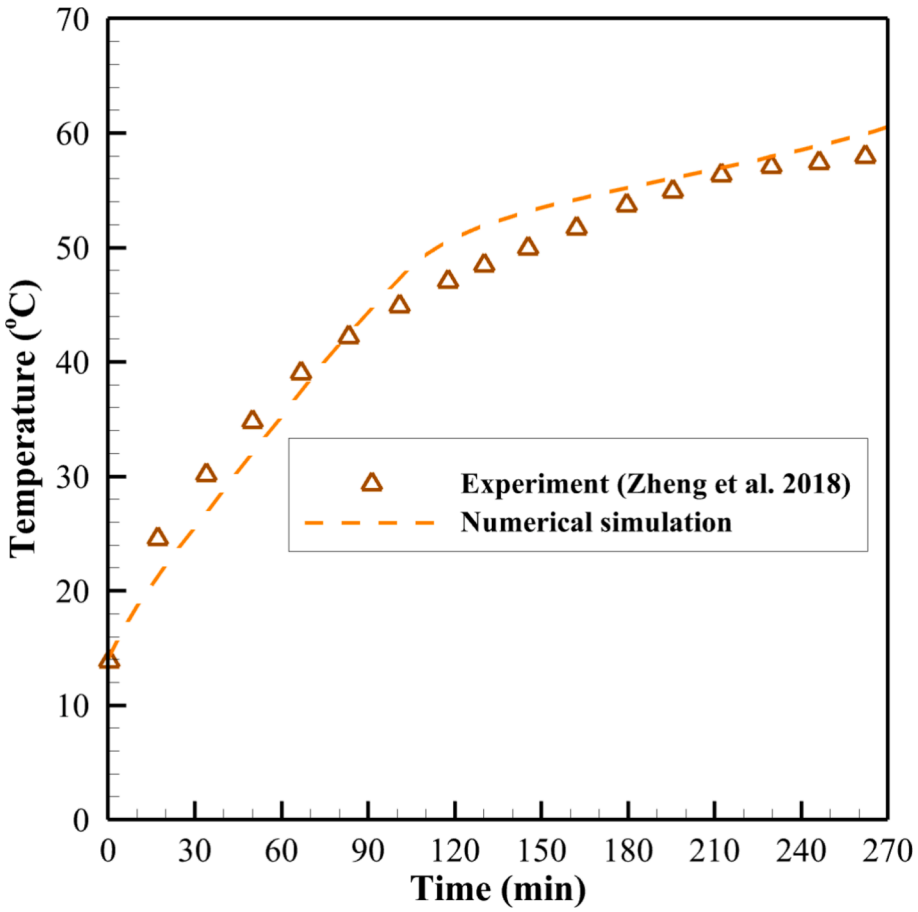

Fig. 8. Comparison of temperature at the enclosure wall.

Table 3
Detail of the numerical experiment cases.

Case	Goal	N	λ	HL_0	HL_1	HL_2	Melting MVF = 0.9		Solidification MVF = 0.1	
							Time (s)	Q_{store} (kJ/m)	Time (s)	Q_{store} (kJ/m)
G1	Petal number	4	0.5	H/2	H	H	1807	5579.5	2087	619.9
G2		5	0.5	H/2	H	H	1774	5579.7	2034	620
G3		6	0.5	H/2	H	H	1741	5580	1991	620
G4		7	0.5	H/2	H	H	1716	5580.3	1925	620
G5		8	0.5	H/2	H	H	1687	5580.6	1929	620.1
G6	Petal amplitude	8	0.3	H/2	H	H	1867	5579.7	2161	620
G7		8	0.4	H/2	H	H	1771	5580.1	2043	620
G8		8	0.6	H/2	H	H	1614	5581.3	1810	620.1
G9	Petal positions	8	0.6	H/2-D	H	H	1981	5581.3	2944	620.1
G10		8	0.6	H/2-D	H-D	H	3034	5581.3	6001	620.1
G11		8	0.6	H/2-D	H-D	H-D	4061	5581.3	10,008	620.1
G12		8	0.6	H/2	H-D	H-D	2902	5581.3	5692	620.1
G13		8	0.6	H/2 + D	H-D	H-D	2758	5581.3	3833	620.1
G14		8	0.6	H/2-D	H-D	H + D	2120	5581.3	3179	620.1
G15	Reference cases	0	0	H/2	H	H	2137	5579.1	2482	619.9
G16		0	0	H/2-D	H-D	H + D	2634	5579.1	4103	619.9

Fig. 9 indicates that the simple circular tube significantly delays both melting and solidification processes. In contrast, the petal geometry accelerates these phase transitions. Increasing the number of petals enhances both melting and solidification, thus reducing the overall phase transition time. This results in shorter thermal charging and discharging durations. However, the differences observed among varying petal numbers are relatively modest. This minor variation is primarily due to the metal foam in the domain, which rapidly redistributes local heat throughout its structure, swiftly transferring heat into the PCM.

Fig. 10 shows that at the initial stages (t = 300 s), circular liquid regions form around each tube and quickly occupy the gaps between petals. Subsequently, these circular regions expand and merge with neighboring liquid areas to create larger liquid domains. When petal shapes are used, the initial liquid region is significantly larger compared to a simple circular tube. This occurs because the petal structure extends heat transfer more broadly due to the amplitude of petals. Consequently, as observed in the *MVF* graphs (Fig. 9), the performance difference between the simple tube (G15) and petal tubes becomes apparent at the beginning and persists throughout the phase transition process.

At the intermediate stage of melting (t = 1500 s), a large unified

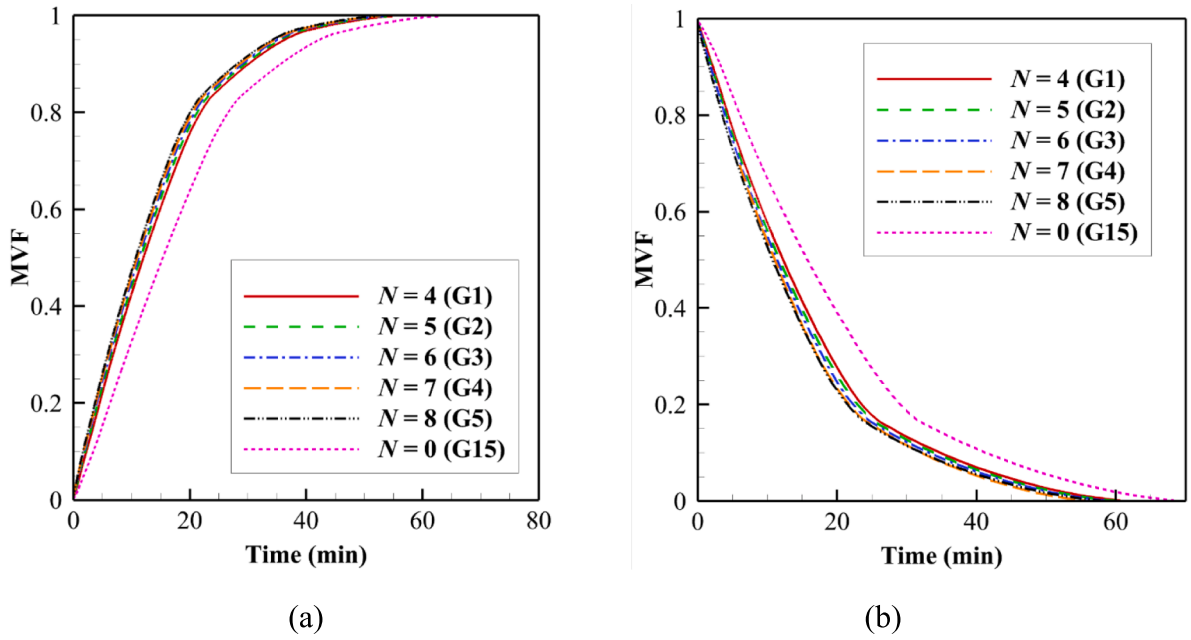

Fig. 9. The impact of petal number (N) on the melting faction history during (a) melting and (b) solidification process.

region of liquid PCM is evident, although some solid PCM regions remain at the top and bottom areas. Initially, the temperature distribution displays a more circular pattern due to the elliptical nature of the heat equation, indicating that conduction is the dominant heat transfer mechanism at this stage.

In the final melting stages ($t = 2100$ s), the phase change progresses upward, driven primarily by natural convection, while the bottom region stays predominantly solid. The impact of natural convection is clearly visible in the temperature contours at both intermediate and final stages ($t = 1500$ s and $t = 2100$ s). Hot liquid PCM plumes rise above each heated tube, enhancing vertical heat transport. By the end of the melting process, significant temperature gradients persist only at the bottom regions, consistent with these areas retaining residual solid PCM.

Cases with a higher petal count (such as G5) achieve slightly more effective melting at the top regions than those with fewer petals (such as G1). This improvement stems from the increased heat transfer surface area available with more petals. Nevertheless, due to the effective heat redistribution provided by the metal foam, the advantage conferred by additional petals quickly diminishes.

Fig. 11 shows how varying petal amplitudes influence the melting (Fig. 11a) and solidification (Fig. 11b) processes. Fig. 12 further illustrates the corresponding liquid fraction and temperature distributions (isotherms) during melting.

As demonstrated in Fig. 11, changing the petal amplitude significantly affects the phase transition behavior. An increased petal amplitude accelerates both melting and solidification processes from the very beginning. Notably, tubes with petal shapes have a clear advantage over simple tubes. The simple tubes (G15) show a considerable delay in phase transition compared to petal-shaped tubes. The influence of petal amplitude becomes particularly pronounced during the middle phase of the transition, around 20 min when most of the enclosure transitions into liquid during melting and solid during solidification.

Examining the liquid fraction and isotherms in Fig. 12 reveals that the region surrounding the petals quickly melts and forms a circular liquid zone at the initial stage ($t = 300$ s). Tubes with high petal amplitude (G8) create larger liquid regions compared to those with lower amplitude (G6). This occurs because larger amplitude petals extend further into the PCM (phase change material) domain, initiating melting over a wider area. Importantly, using petal tubes does not change the quantity of PCM in the domain, as both simple and petal tubes have equal surface areas. However, petal-shaped tubes melt the surrounding PCM more rapidly, quickly bridging gaps between petals, resulting in an early notable difference in MVF curves.

As melting progresses, the individual molten regions merge, forming extensive liquid areas. Petals with higher amplitude (G8) generate larger molten regions, reducing the size of solid regions between tubes compared to lower amplitude petals (G6). At this stage, differences in MVF curves become significant. The isotherms also indicate robust formation of thermal plumes in both cases, with G8 generating stronger and more aggressive upward convection due to its larger heat transfer area.

At the intermediate stage ($t = 1500$ s), all local liquid regions combine into a single extensive liquid domain, although solid regions remain at the top and bottom. By this point, the immediate local impact of petal amplitude diminishes somewhat, yet its overall advantage in providing enhanced heat transfer surface area remains clear. Enhanced upward movement of hot PCM liquid for G8 further underscores better natural convection compared to G6.

At the final stage of melting ($t = 2100$ s), most of the top region is molten, and the differences in MVF between G6 and G8 significantly reduce. Hot liquid accumulates predominantly at the top, leaving only the bottom region partially solid. This residual solid region eventually melts through minimal liquid PCM flow and conduction from the lower petals.

4.2. *Geometrical placement of petals*

Figs. 13 and 14 focus on the impact of petal tube locations on the phase change process, while Fig. 15 shows the corresponding liquid fraction and temperature distributions (isotherms) during melting for three cases with different petal tube location configurations (G9, G11, and G16). Figs. 13 and 14 reveal a notable difference in phase transition behavior as the petal tube locations change. Here, G5 serves as the typical reference case, as discussed in previous sections. In G9, the tube bundles are shifted downward by a distance D. The precise location parameters (HL_0, HL_1, HL_2) for all cases are detailed in Table 3. In G10, all tubes are first shifted downward, and then the middle tube is shifted further downward by D. G11 is similar to G10, but the top tube is also

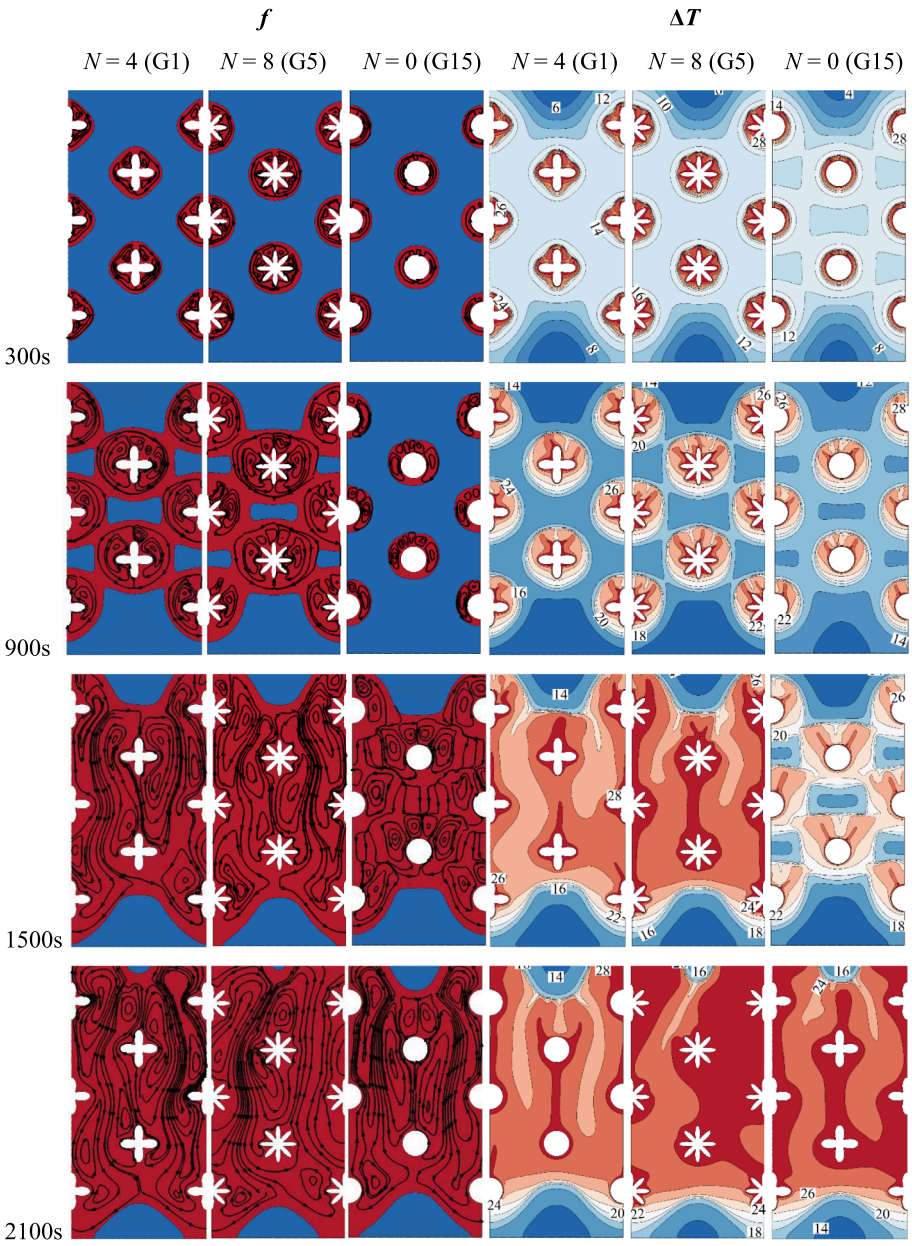

Fig. 10. Impact of petal number (N) on the liquid field (f) and temperature field (ΔT) at various times during the melting process.

shifted downward by D. Finally, G16 is plotted as a reference case with a simple tube layout similar to G10, but the top tube is shifted upward by D.

From Fig. 13, all petal tube cases show similar phase transition behavior during the early stages, up to about 600 s. Only case G16 shows some differences, which can be attributed to its simple tube shape — a factor discussed earlier. The similarity among the petal cases at early phase transition stages, regardless of tube location, is because each petal initially melts or solidifies only its surrounding area. This observation is supported by the melting maps in Fig. 15, where at $t = 300$ s, each petal has melted a local region, and the combined molten area is nearly the same across all cases.

As time progresses to $t = 900$ s (15 min), the molten PCM regions expand and begin to merge. At this stage, notable differences emerge between the molten patterns of cases G9 and G11, though the total liquid areas remain comparable. These differences in molten region patterns and tube locations set the stage for more significant disparities at later times. Shifting all tubes downward (G9) creates a well-distributed layout, allowing the bottom tube to melt the lower region effectively. However, shifting the top tube downward (G11) does not provide an advantage and, in fact, weakens natural convection and the progression of melting at the top.

The simple tube (G16) melts the domain with a noticeable delay due to its limited heat transfer surface compared to petal tubes. However, placing a simple tube correctly at both the bottom and top offers good melting distribution across the domain. As time advances ($t = 1500$ s and $t = 2100$ s), the disadvantages of shifting the top petal tube downward in G11 become more pronounced compared to G9. By $t = 2100$ s, cases G9, G11, and G16 have melted the entire bottom region, but the top region remains largely solid. G9 performs well in melting the top area because it has a tube positioned near the top.

The isotherms show strong natural convection effects in both petal cases (G9 and G11) during the final melting stages. The upward extension of hot temperature plumes is less pronounced in G16 (simple tube) compared to the petal tubes, but because G16 has a well-placed top tube, its performance is comparable to G9 and even surpasses G11. Moving

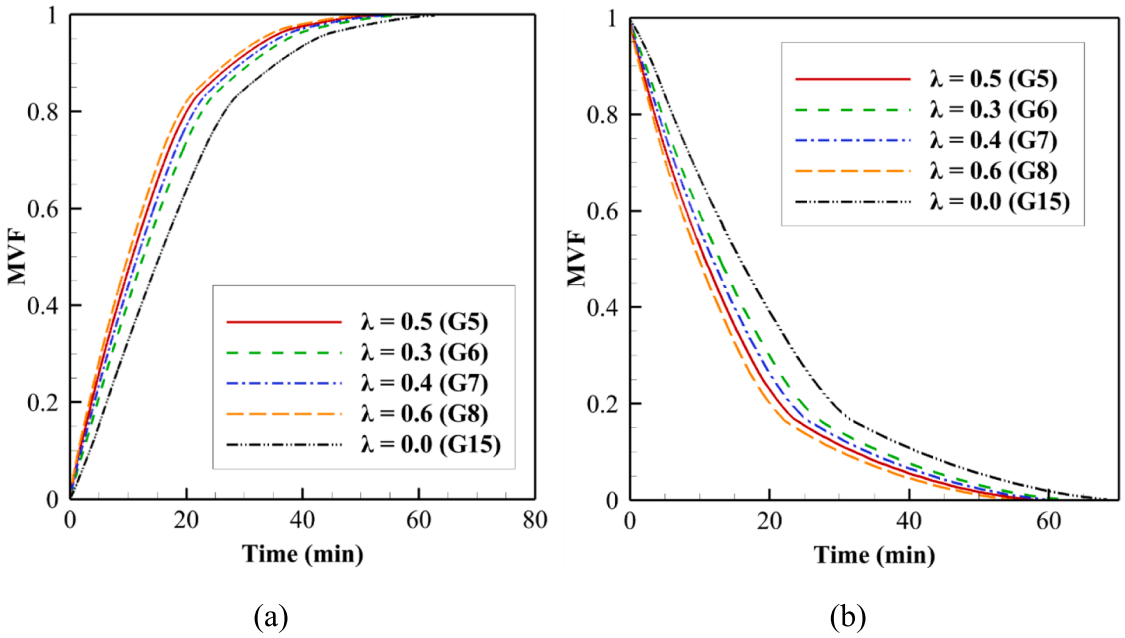

Fig. 11. The impact of petal amplitude (λ) on the melting faction history during (a) melting and (b) solidification process.

the bottom and middle tubes further downward while keeping the top tube at the bottom leads to Case 14. Although this setup improves final-stage melting, it still does not match the performance of Case 5, which benefits from a uniform tube distribution with a slight downward shift ($HL_0 = H/2$).

4.3. Overall analysis of investigated cases

Fig. 16 depicts the required melting time for melting (MVF = 0.9) and the required time for solidification ($MVF = 0.1$) in a bar chart format. The data in Fig. 16a shows that increasing the number of petals from N = 4 to N = 8 (Cases G1 to G5) consistently reduces the melting time, with a reduction from 1807 s (4 petals) to 1687 s (8 petals), representing a ~6.6 % decrease. When examining the effect of petal amplitude (G6–G8), the case with higher amplitude ($\lambda = 0.6$) remarkably decreases the melting time to 1614 s, compared to 1867 s for $\lambda = 0.3$, achieving a ~13.6 % reduction.

The most dramatic variations are observed in the petal tube location configurations (G9–G14). For example, G9 (shifted position) increases the melting time to 1981 s (~17.5 % longer than G5), while G10–G11 further increase the time dramatically, with G11 reaching 4061 s—more than 140 % longer compared to the baseline G5. Thus, as observed in Figs. 13 and 14, petal tube placement significantly affects the phase change heat transfer. For reference, the cases without petals (G15, G16) show moderate melting times (2137–2634 s), longer than the optimal petal cases (G5, G8). Thus, proper petal configurations enhance heat transfer efficiency.

Fig. 16b focuses on the solidification process. Here, increasing the number of petals (G1–G5) reduces the solidification time from 2087 s (4 petals) to 1929 s (8 petals), an ~ 7.5 % decrease. For petal amplitude (G6–G8), higher amplitude ($\lambda = 0.6$, G8) reduces the time to 1810 s compared to 2161 s at $\lambda = 0.3$ (~16.2 % improvement). However, changes in the petal tube location (G9–G14) show large increases in solidification time, with G9 reaching 2944 s (~52.6 % longer than G8) and G11 peaking at 10,008 s, a 450 % increase compared to G8. These extreme increases indicate that tube positioning strongly impacts the freezing front progression. The reference cases without petals (G15, G16) again show longer times (2482–4103 s), which shows the beneficial effect of optimized petal configurations.

Considering Table 3, across all the investigated cases, the stored energy values during melting (Q_{store} at $MVF = 0.9$) remained remarkably consistent, ranging narrowly between approximately 5579.1 kJ/m to 5581.3 kJ/m. This indicates that, despite variations in petal number, amplitude, or tube positions, the total amount of heat stored in the system during the melting process is largely unaffected. This is because the amount of PCM and metal foam is fixed. The small variations are due to temperature non-uniformity and, consequently, the sensible heat variations. During solidification ($MVF = 0.1$), Q_{store} similarly shows no major change, staying consistently near ~620–620.1 kJ/m across all configurations. This reinforces that geometry and petal shape arrangements mainly influence the rate of heat transfer, not the amount of thermal energy stored or released.

Fig. 17 depicts the liquid fraction and isotherms throughout the solidification process for the best (G8), worst (G11), and reference (G15) cases based on tube location configurations. In cases G8 and G11, the amplitude and number of petals are fixed; the only variable is the arrangement of the petal tube locations.

In the early stages of solidification ($t = 300$ s), thin solid layers form around the petals and quickly fill the gaps between them. For the reference case with a simple tube (G15), the solid region is comparatively small due to the limited surface area available for heat transfer. The solidification curves shown in Figs. 13 and 14 reflect similar early-stage behaviors for these cases. As time progresses, the solid regions expand, and larger solid clusters form, trapping some molten zones ($t = 900$ s).

By the mid-stage of solidification ($t = 1500$ s), the solidification front moves downward because the colder liquid tends to settle at the bottom, making the upper regions the last to freeze. The isotherms reveal that natural convection flows are generally weak during this phase. However, the downward convection contributes to the solidification of the bottom region. Notably, the presence of a tube positioned toward the top, as seen in case G8, aids in the solidification of the upper region. In the final stages of solidification, overall heat transfer slows down because the cold tubes must draw heat through conduction, working across increasingly thick solid layers.

5. Artificial intelligence analysis

Accurately calculating heat transfer during phase transitions, such as melting and solidification, often involves extremely demanding

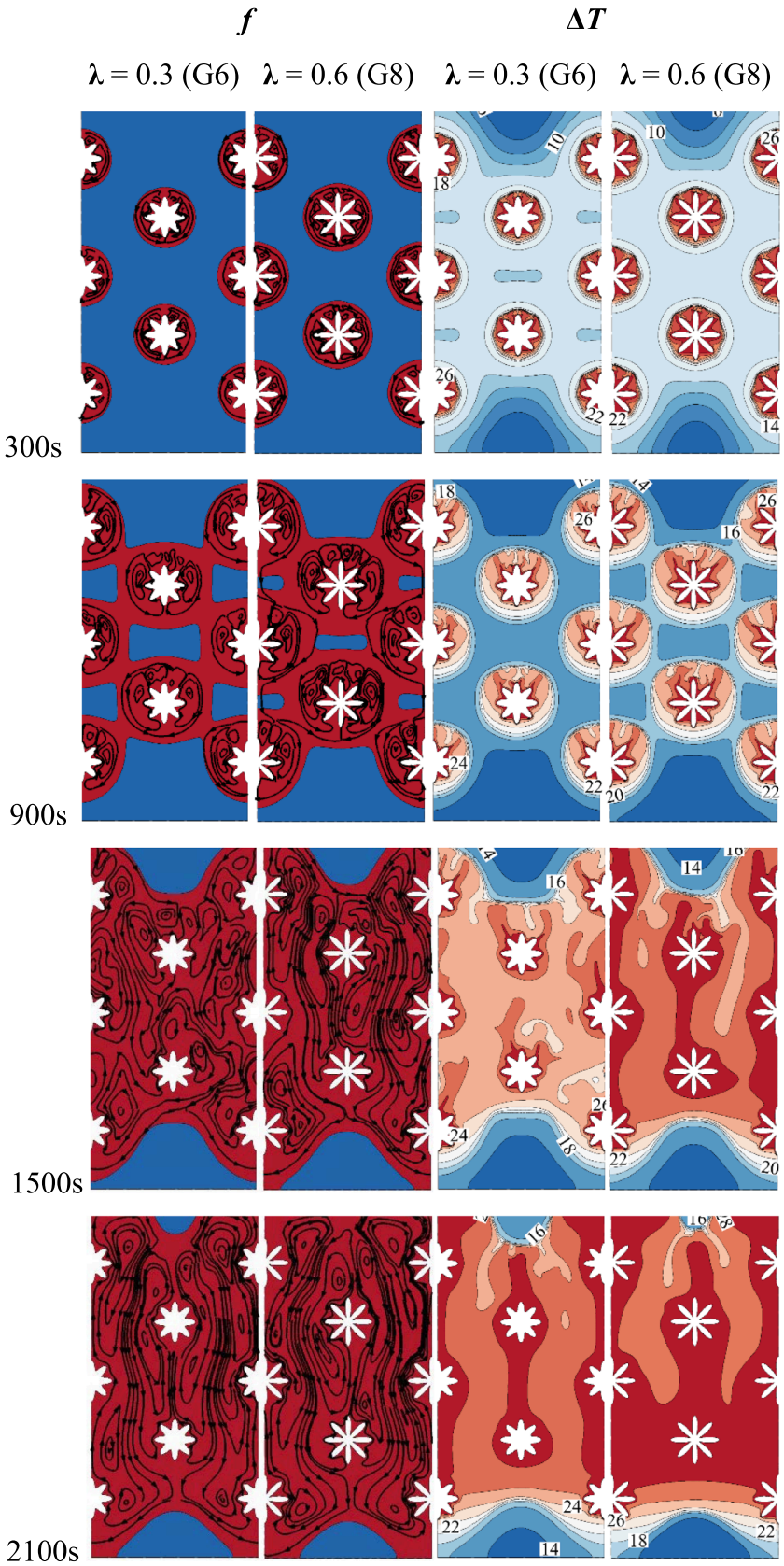

Fig. 12. Impact of petal amplitude (λ) on the liquid field (f) and temperature field (ΔT) at various times during the melting process.

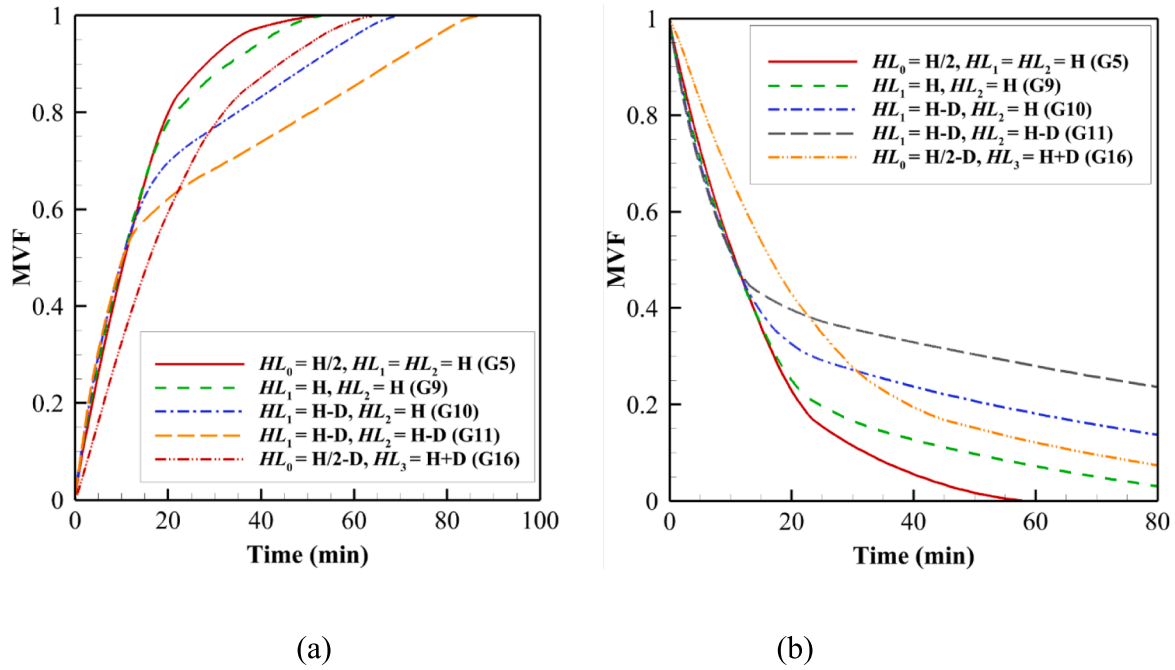

Fig. 13. The impact of the location of the petal tubes on the melting faction history during (a) melting and (b) solidification process when H_0=$H/2$-D.

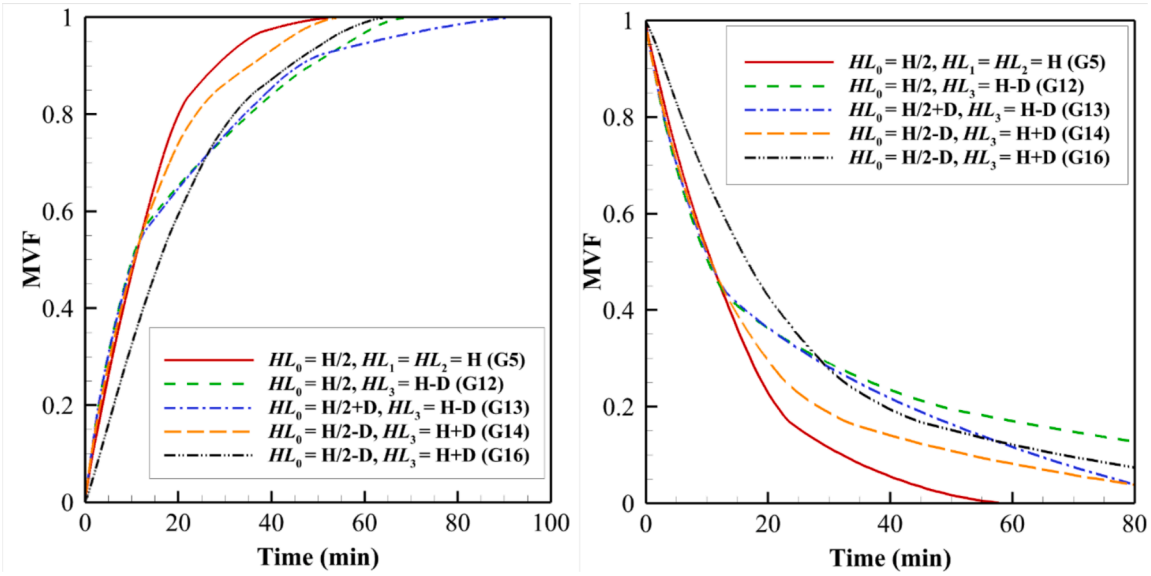

Fig. 14. The impact of the location of the middle and bottom petal tubes (HL_0 and HL_1) on the melting faction history during (a) melting and (b) solidification process.

computations. Even analyzing a single configuration can require several days due to the intense processing load. Consequently, it becomes unfeasible to carry out the numerous simulations necessary to systematically examine how different design parameters influence PCMs using conventional computing resources.

To overcome this computational barrier and still perform broad design explorations, researchers now employ Artificial Neural Networks (ANNs) to approximate the thermal dynamics of these systems. The ANN framework applied here comprises three hidden layers, each containing 15 neurons, all utilizing the sigmoid activation function. A visual representation of the network layout is provided in Fig. 18.

To construct the training dataset, a total of 161,519 data records were generated from simulation runs. This dataset is publicly available through Mendeley at the following link [50]:

The dataset is structured with seven input (independent) variables and one output (dependent) variable, all summarized in Table 4, which also presents the corresponding value ranges for each. Before initiating the training process, the dataset underwent normalization using the StandardScaler approach [51], where each data point x was transformed according to the equation:

$$normal\_x = \frac{x - \mu}{\sigma} \tag{14}$$

Here, μ represents the mean, σ the standard deviation, and normalized_x the standardized value. To ensure robust model performance, the data was shuffled and split, reserving 70 % for training while the remaining 30 % was equally divided between validation and testing. The ANN was trained over 1000 epochs using a batch size of eight. The

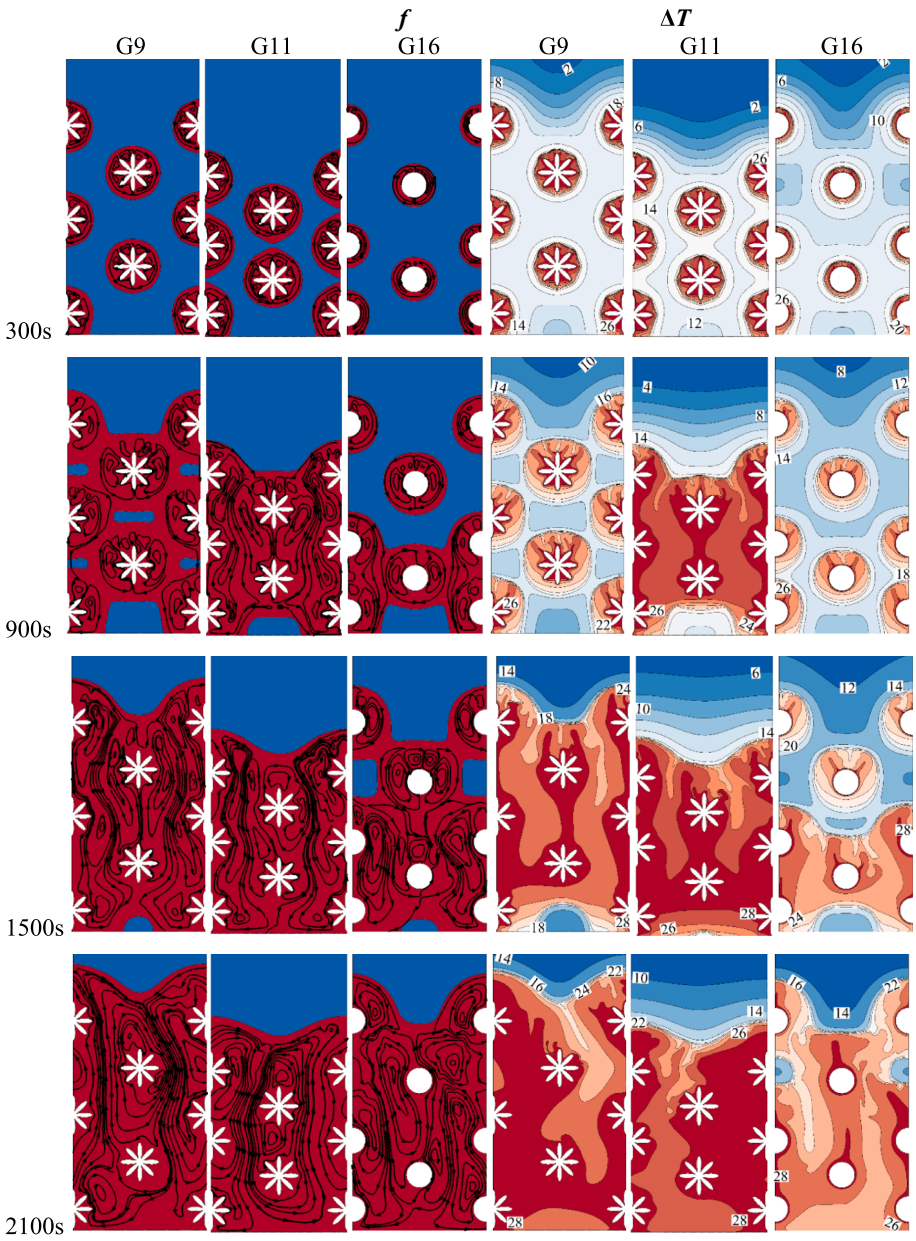

Fig. 15. Impact of petal tube locations on the liquid field (f) and temperature field (ΔT) at various times during the melting process.

training objective was to minimize the Mean Squared Error (MSE) loss function, employing the Adam optimization algorithm [52]. Upon completion, the model achieved exceptionally low validation and test losses of 4.84×10^{-6} and 5.77×10^{-6}, respectively, demonstrating high predictive accuracy. Fig. 19a shows the steady reduction in MSE over the course of training for both the training and validation datasets, highlighting the model's continuous improvement. Fig. 19b presents a comparison between the predicted outcomes and actual test data, yielding an impressive coefficient of determination (R^2) of 0.999, confirming the model's reliability.

Leveraging the trained ANN, Additional studies were undertaken to evaluate the impact of two key geometric parameters—petal location HL_0/D and petal amplitude λ—on the *MVF* during both melting (Fig. 20a) and solidification (Fig. 20b) phases. Results indicate that increasing petal amplitude consistently enhances the *MVF* during melting, leading to improved thermal performance. During solidification, the most favorable (i.e., lowest) *MVF* values, indicating superior solidification efficiency, are observed at the highest petal amplitudes. Therefore, amplifying petal amplitude proves beneficial across both phase change scenarios.

In contrast, while increasing HL_0/D improves melting performance, the solidification process exhibits an optimal range centered around $HL_0/D = 1.4$, beyond which improvements taper off. These insights, derived from ANN-generated contour plots, highlight the hybrid modeling approach's effectiveness in capturing complex system behavior and guiding design optimizations without the need for exhaustive direct simulations.

6. Conclusions

The melting and solidification over a bundle of petal-shaped tubes embedded in a metal foam-PCM domain was addressed. The LTNE model, which consists of a temperature field for PCM and a temperature field for metal foam, was used to model the phase change heat transfer in the system. The natural convection effects were taken into account in the liquid PCM domains. The enthalpy-porosity approach was used to model the fluid flow and phase change. The impact of the number of petals, the petal amplitudes, and the geometrical location of petal tubes was

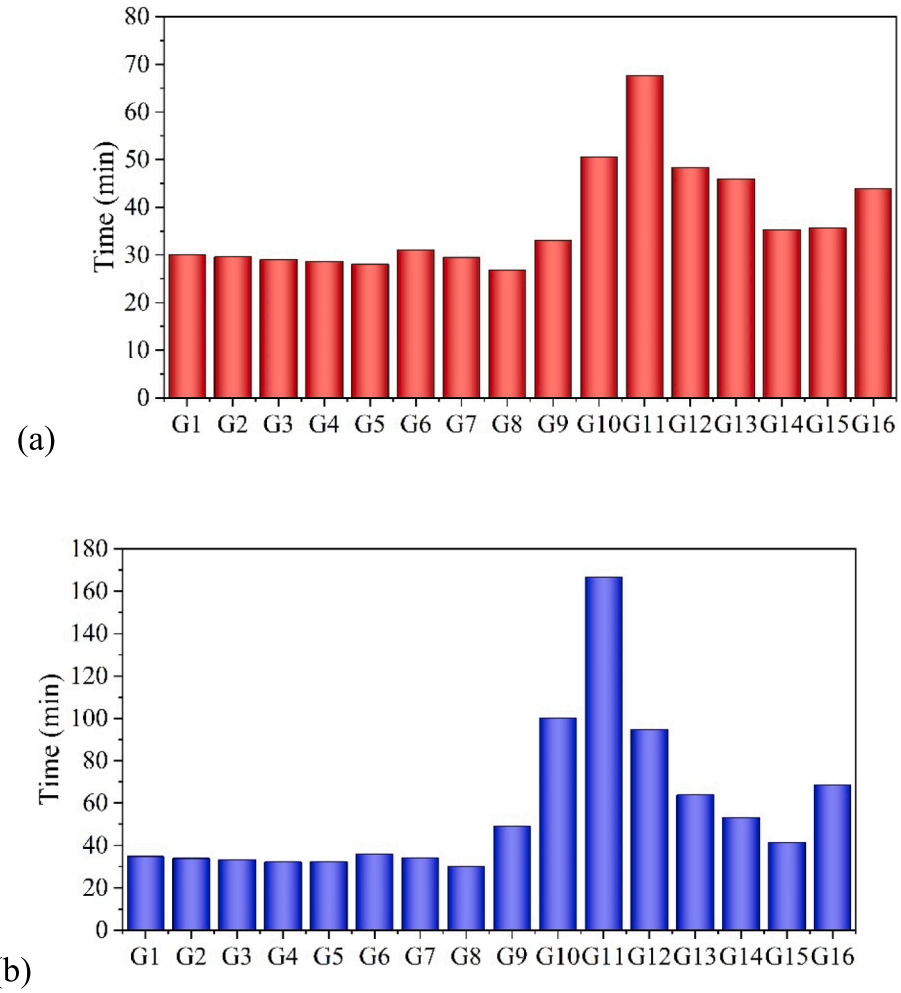

Fig. 16. The bar chart of required time for (a) *MVF* = 0.9 during the melting process and (b) *MVF* = 0.1 during the solidification process.

investigated on the melting and solidification time and the stored/released heat. Using the simulated cases, a dataset of time-dependent melting and solidification behavior for various control parameters was created, which consisted of 161,519 records. An AI technique based on ANNs was used to map the control parameter to the phase change. The trained DNN was able to successfully understand the physical behavior of the system. Then, the trained DNN was used to further predict the influence of design parameters on the melting behavior of the system. The main outcomes of the study can be summarized as follows:

- It was found that petal-shaped geometries significantly enhance both melting and solidification rates when compared to simple circular tubes. While increasing the number of petals expands the available heat transfer surface, the resulting performance gains are moderate because the metal foam effectively redistributes heat throughout the domain. During the early phase of melting, circular liquid regions develop and merge rapidly, with petal designs creating larger initial melted zones. At later stages, natural convection becomes the dominant heat transfer mechanism, moving residual solids to the bottom and largely equalizing performance across different petal configurations.
- Increasing the petal amplitude (λ) was found to notably improve phase change performance. Specifically, raising λ from 0.3 (G6) to 0.6 (G8) reduced melting time from 1867 s to 1614 s, yielding a ~13.6 % improvement. Likewise, solidification time dropped from 2161 s to 1810 s, an enhancement of ~16.2 %. After approximately 20 min, over 90 % of the PCM becomes molten, and the performance differences between lower- and higher-amplitude petal configurations diminish in the later stages.
- The arrangement of petal tube locations critically influences phase change behavior. Initially (at t = 300 s), all configurations exhibit similar local melting patterns, but as time progresses and molten regions merge, design differences become pronounced. For example, shifting the tube bundle downward (G9) increased melting time to 1981 s (~17.5 % longer than G5), whereas shifting both the middle and top tubes downward (G11) raised melting time dramatically to 4061 s, over 140 % longer. Solidification time in G11 reached 10,008 s, representing a 450 % increase compared to G8. Simple circular tubes without petals (G15, G16) showed moderate phase change times but consistently underperformed relative to well-optimized petal configurations.
- Despite notable differences in melting and solidification times, the total thermal energy stored remained remarkably consistent across all cases. During melting, Qstore ranged narrowly between ~5579 and 5581 kJ/m, while during solidification, it stayed near ~620–620.1 kJ/m. This consistency indicates that while geometric configurations affect the rate of heat transfer, they do not significantly change the amount of thermal energy stored or released, as the quantities of PCM and metal foam remain fixed across designs.
- ANN models provided powerful predictive insights into system behavior. The ANN-generated contour plots confirmed that increasing λ consistently improves melting and solidification efficiency, while the optimal petal location parameter (HL_0/D) for solidification centers around 1.4. Beyond this point, further

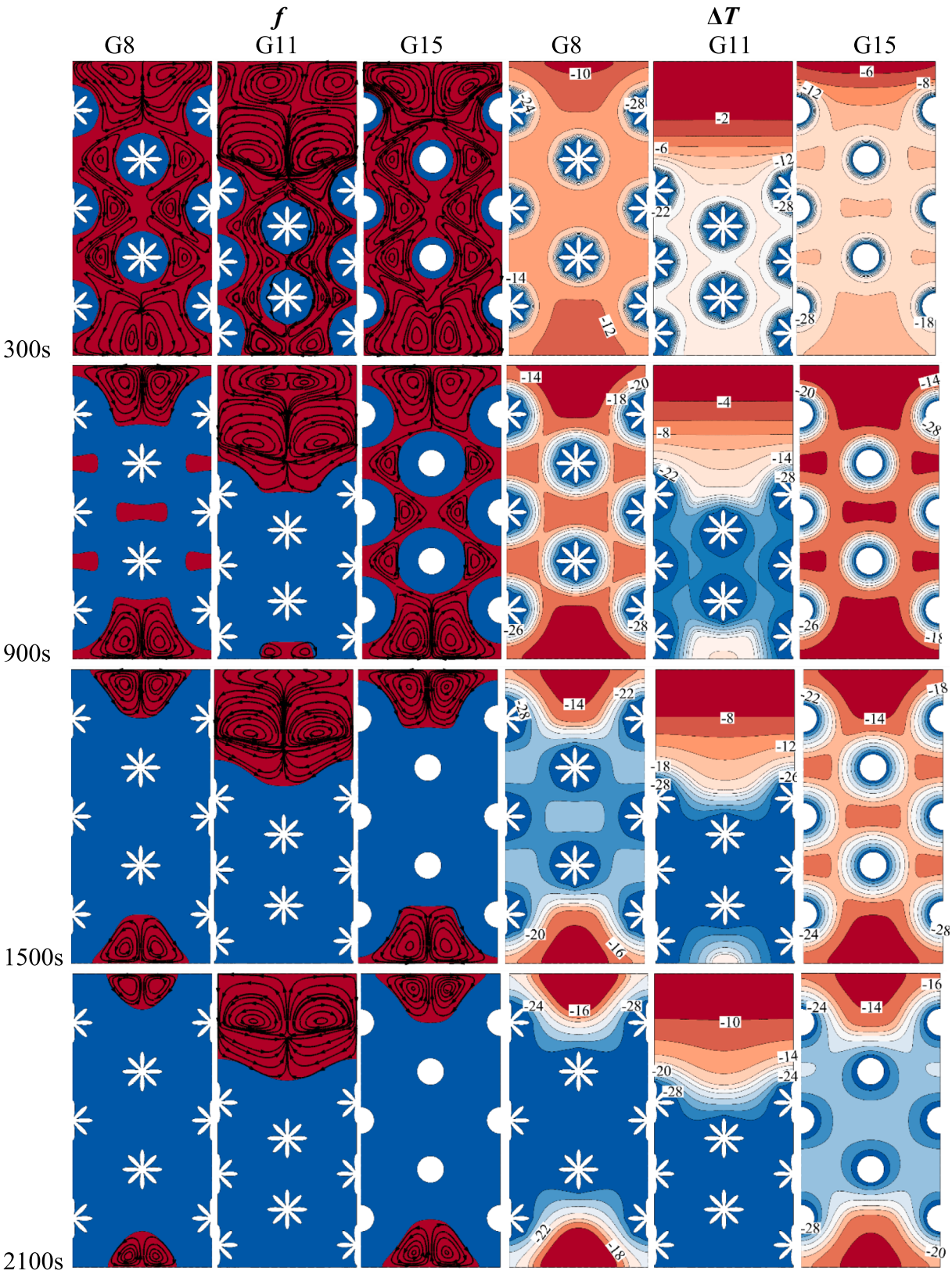

Fig. 17. A comparison of the best (G8) and worst (G11) petal configuration tubes and reference cases (G15) for the liquid filed (*f*) and temperature field (ΔT) at various times during the solidification process.

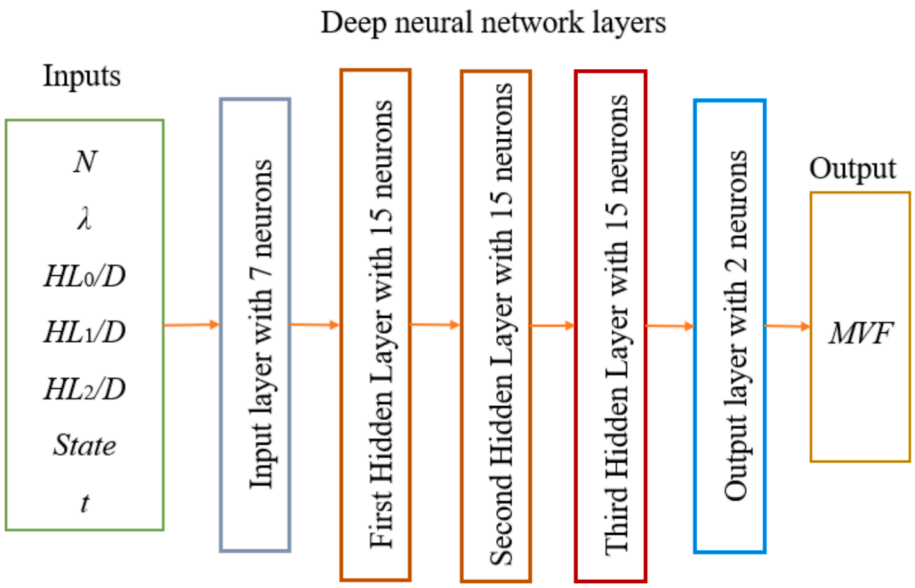

Fig. 18. The framework of the applied neural networks for training the physical behavior of the energy storage system.

Table 4
Catalog of ANN inputs and results.

ANN Inputs		Range
Symbol	Description	
N	Petal number	$4 < N < 8$
λ	Petal amplitude	$0.3 < \lambda < 0.6$
HL_0/D	Petal position 1	$5/6 < HL_0/D < 17/6$
HL_1/D	Petal position 2	$8/3 < HL_1/D < 11/3$
HL_2/D	Petal position 3	$8/3 < HL_1/D < 14/3$
State	Solidification = 0 Melting = 1	0, 1
t	Phase transition time (s)	$0 < t < 17000$
ANN Outputs		
Symbol	Description	
MVF	Melting volume fraction	$0 < MVF < 1$

performance gains taper off. The ANN approach effectively captures complex thermal interactions and serves as a valuable design optimization tool, reducing the need for exhaustive, time-intensive direct simulations and streamlining the exploration of advanced phase change system designs.

The results of the present study showed that the location of tube bundles and petal shape can effectively impact the melting and solidification time. The DNN was able to successfully capture the system behavior. Therefore, the future studies can explore the integration of machine-learning-based optimization algorithms, such as reinforcement learning or genetic algorithms, to automate design improvements and parameter tuning. In addition, the developed methodology can be extended to other PCM-based energy systems, including solar thermal collectors, battery thermal management, and thermal regulation in buildings. Applying the DNN framework to more complex geometries and transient load conditions will further expand its utility in practical,

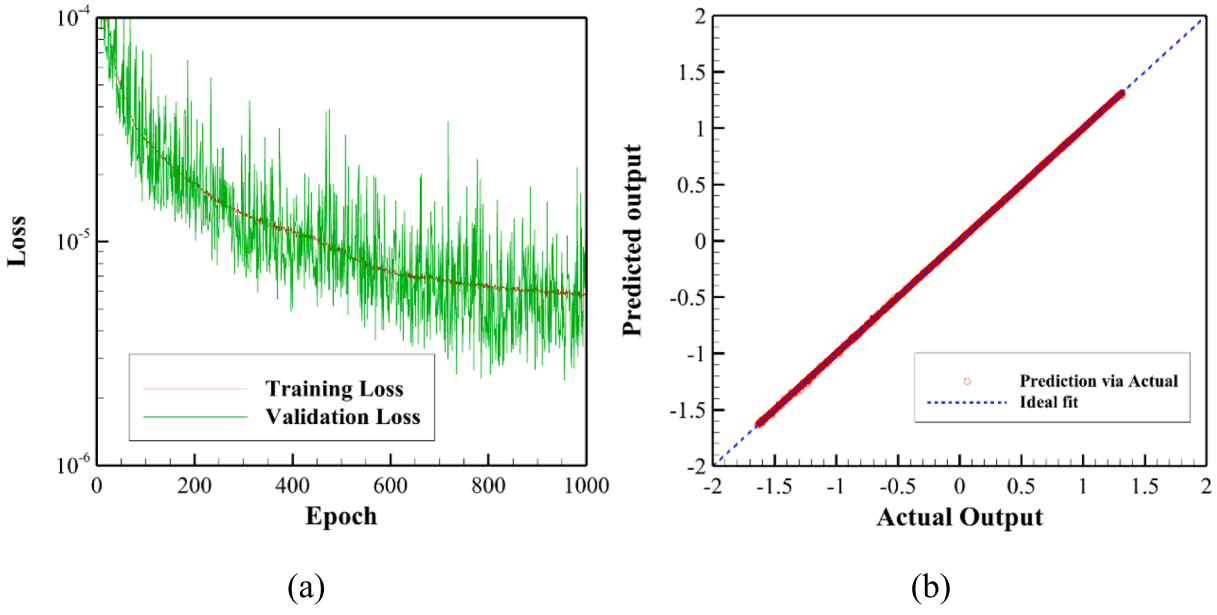

Fig. 19. The model training analysis for (a) the training and validation loss values over epochs and (b) a comparison of predicted and actual data.

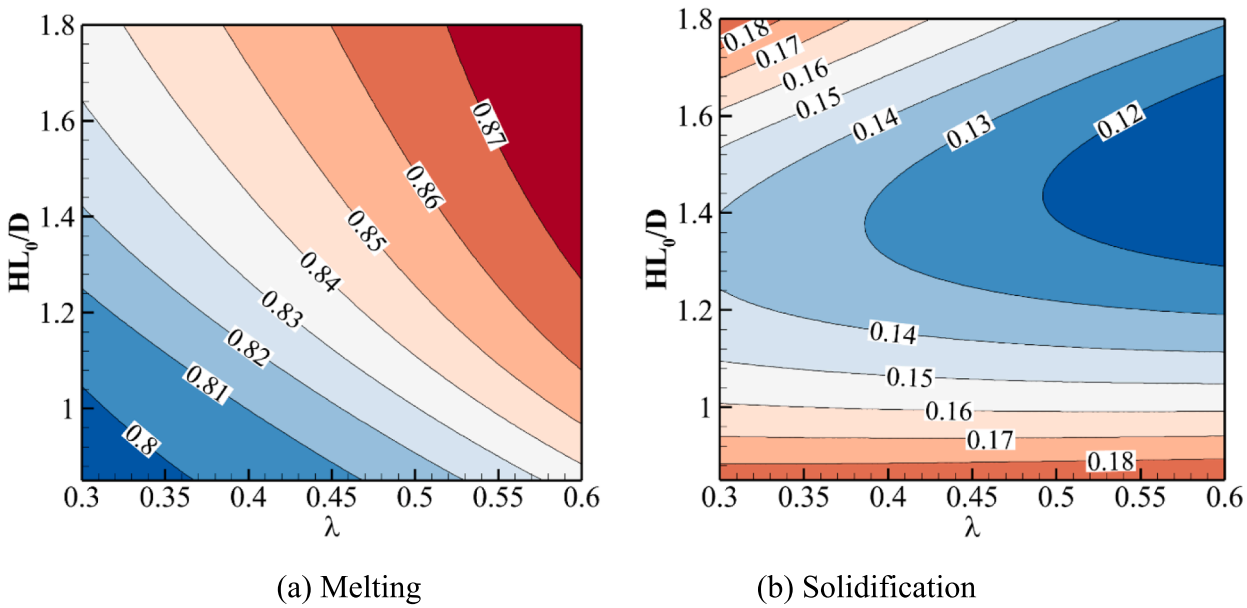

Fig. 20. The maps of MVF for a range of HL0/D and petal amplitude λ when N = 8, t = 1500 s, HL_1/D = 11/3, and HL_2/D = 11/3.

real-world energy storage applications.

CRediT authorship contribution statement

Jana Shafi: Writing – review & editing, Writing – original draft, Visualization, Software, Methodology, Funding acquisition, Formal analysis, Data curation, Conceptualization. **Obai Younis:** Writing – original draft, Software, Resources, Investigation, Formal analysis. **Saeed Tiari:** Writing – review & editing, Writing – original draft, Validation, Methodology, Investigation, Data curation, Conceptualization. **Mohammad Ghalambaz:** Writing – review & editing, Writing – original draft, Visualization, Validation, Supervision, Formal analysis.

Funding

The authors extend their appreciation to Prince Sattam bin Abdulaziz University for funding this research work through the project number (2024/01/31559).

Declaration of competing interest

The authors declare that they have no known competing financial interests or personal relationships that could have appeared to influence the work reported in this paper.

Acknowledgment

The authors extend their appreciation to Prince Sattam bin Abdulaziz University for funding this research work through the project number (2024/01/31559).

References

[1] K.Y. Leong, S. Hasbi, B.A. Gurunathan, State of art review on the solidification and melting characteristics of phase change material in triplex-tube thermal energy storage, J. Storage Mater. 41 (2021) 102932.
[2] C.A. Saleel, A review on the use of coconut oil as an organic phase change material with its melting process, heat transfer, and energy storage characteristics, J. Therm. Anal. Calorim. 147 (2022) 4451–4472.
[3] C. Zhao, M. Opolot, M. Liu, J. Wang, F. Bruno, S. Mancin, K. Hooman, Review of analytical studies of melting rate enhancement with fin and/or foam inserts, Appl. Therm. Eng. 207 (2022) 118154.
[4] M. Rogowski, R. Andrzejczyk, Recent advances of selected passive heat transfer intensification methods for phase change material-based latent heat energy storage units: a review, Int. Commun. Heat Mass Transfer 144 (2023) 106795.
[5] S. Tian, J. Ma, S. Shao, Q. Tian, Z. Wang, Y. Zhao, B. Tan, Z. Zhang, Z. Sun, Estimation of heat transfer performance of latent thermal energy storage devices with different heat transfer interface types: a review, J. Storage Mater. 86 (2024) 111315.
[6] X.H.K. Le, H.F. Öztop, M.A. Sheremet, Numerical simulation of natural convection in a differentially heated cubical cavity with solid fins, Internat. J. Numer. Methods Heat Fluid Flow 34 (2024) 3369–3392.
[7] M.A. Rahman, R. Zairov, N. Akylbekov, R. Zhapparbergenov, S.M. Hasnain, Pioneering heat transfer enhancements in latent thermal energy storage: Passive and active strategies unveiled, Heliyon 10 (2024).
[8] H.A. Al-Salami, N.S. Dhaidan, H.H. Abbas, F.N. Al-Mousawi, R.Z. Homod, Review of PCM charging in latent heat thermal energy storage systems with fins, Therm. Sci. Eng. Prog. 51 (2024) 102640.
[9] F. Ma, T. Zhu, Y. Zhang, X. Lu, W. Zhang, F. Ma, A review on heat transfer enhancement of phase change materials using fin tubes, Energies 16 (2023) 545.
[10] J. Guo, Z. Liu, B. Yang, X. Yang, J. Yan, Melting assessment on the angled fin design for a novel latent heat thermal energy storage tube, Renew. Energy 183 (2022) 406–422.
[11] C. Nie, Z. Chen, H. Li, X. Liu, J. Liu, Z. Rao, Petal-shaped fin configurations for enhancing phase change material solidification in a horizontal shell and tube thermal energy storage unit, J. Storage Mater. 113 (2025) 115685.
[12] M. Boujelbene, S.A. Mehryan, M. Sheremet, M. Shahabadi, N.B. Elbashir, M. Ghalambaz, Numerical study of a non-Newtonian phase change flow in finned rectangular enclosures, Facta Universitatis, Series: Mechanical Engineering (2024).
[13] B. Buonomo, M.R. Golia, O. Manca, S. Nardini, A review on thermal energy storage with phase change materials enhanced by metal foams, Therm. Sci. Eng. Prog. (2024) 102732.
[14] N.S. Bondareva, M.A. Sheremet, Numerical simulation of heat transfer performance in an enclosure filled with a metal foam and nano-enhanced phase change material, Energy 296 (2024) 131123.
[15] T. Si, W. Cui, T. Ma, L. Lu, Q. Wang, Numerical investigation on thermal performance of phase change materials embedded in functionally graded metal foam, J. Storage Mater. 81 (2024) 110482.
[16] M. Ghalambaz, M. Sheremet, K. Shank, S. Tiari, M. Fteiti, Improving phase change heat transfer in an enclosure partially filled by uniform and anisotropic metal foam layers, Int. J. Heat Mass Transf. 228 (2024) 125678.
[17] Z. Cheng, J. Du, S. Jia, C. Xiao, F. Jiao, Y. Hong, Impact of tube shapes on the energy storage and thermal-hydraulic performances of finned latent heat energy storage systems, Case Stud. Therm. Eng. 67 (2025) 105827.
[18] L. Gao, Y. Deng, S. Liu, F. Ren, M.P. Wan, L. Yang, Design and optimization of a bionic-lotus root inspired shell-and-tube latent heat thermal energy storage unit, Int. J. Heat Mass Transf. 226 (2024) 125437.
[19] J. Hao, X. Wu, C. Ju, X. Wang, F. Hong, X. Du, Bionic-response surface combination optimization method for latent heat storage performance improvement, Appl. Therm. Eng. 248 (2024) 123320.
[20] B. Kurşun, M. Balta, F. Polat, Simultaneous evaluation of charge/discharge times and energy storage/release capacities in multi-tube latent heat energy storage with metal foam-enhanced PCM, J. Storage Mater. 108 (2025) 115090.
[21] H.B. Mahood, M.S. Mahdi, A.H. Sayer, A.A. Khadom, Y. Rghif, A.A. Alammar, L. Sayin, Y. Allouche, Numerical study of thermal performance of a PCM in a

modifying tube-bundle latent heat thermal storage, Therm. Sci. Eng. Prog. 51 (2024) 102622.
[22] M. Ghalambaz, A.H. Eisapour, H.I. Mohammed, M.S. Islam, O. Younis, P.T. Sardari, W. Yaïci, Impact of tube bundle placement on the thermal charging of a latent heat storage unit, Energies 14 (2021) 1289.
[23] M. Ghalambaz, S. Mehryan, A. Veismoradi, M. Mahdavi, I. Zahmatkesh, Z. Kazemi, O. Younis, M. Ghalambaz, A.J. Chamkha, Melting process of the nano-enhanced phase change material (NePCM) in an optimized design of shell and tube thermal energy storage (TES): Taguchi optimization approach, Appl. Therm. Eng. 193 (2021) 116945.
[24] A. Hassan, I.A. Alnaser, A review of different manufacturing methods of metallic foams, ACS Omega 9 (2024) 6280–6295.
[25] H. Cheradi, Z. Haddad, F. Iachachene, K. Mansouri, M. Arıcı, A comprehensive numerical study on melting performance in a storage cavity with partial metal foam integration: design and economic assessment, J. Storage Mater. 85 (2024) 110985.
[26] Nishiyama's heat exchangers?featuring technology for improved heat transfer performance, in, Vol. 2025, Nishiyama Seisakusho Co., 2025.
[27] S. Mehryan, K. Raahemifar, S.R. Ramezani, A. Hajjar, O. Younis, P. Talebizadeh Sardari, M. Ghalambaz, Melting phase change heat transfer in a quasi-petal tube thermal energy storage unit, PLoS One 16 (2021) e0246972.
[28] M. Mozaffari, K. Hajlaoui, O. Younis, A. Ahmed, D.M. Khidhir, A. Hajjar, M. Ghalambaz, N.H. Alrasheedi, Thermal performance and melting behavior of partially funnel-shaped anisotropic copper foam/paraffin PCM within an LHTES, Heat Transfer (2025).
[29] J. Shafi, M. Ghalambaz, M. Fteiti, M. Ismael, M. Ghalambaz, Computational modeling of latent heat thermal energy storage in a shell-tube unit: using neural networks and anisotropic metal foam, Mathematics 10 (2022) 4774.
[30] A.A. Nnanna, A. Haji-Sheikh, K.T. Harris, Experimental study of local thermal non-equilibrium phenomena during phase change in porous media, Int. J. Heat Mass Transf. 47 (2004) 4365–4375.
[31] S. Zhang, Y. Yao, Y. Jin, Z. Shang, Y. Yan, Heat transfer characteristics of ceramic foam/molten salt composite phase change material (CPCM) for medium-temperature thermal energy storage, Int. J. Heat Mass Transf. 196 (2022) 123262.
[32] M. Ghalambaz, A.A. Melaibari, A.J. Chamkha, O. Younis, M. Sheremet, Phase change heat transfer and energy storage in a wavy-tube thermal storage unit filled with a nano-enhanced phase change material and metal foams, J. Storage Mater. 54 (2022) 105277.
[33] D.A. Nield, A. Bejan, Convection in Porous Media, Springer, 2006.
[34] Y. Yao, H. Wu, Z. Liu, Direct simulation of interstitial heat transfer coefficient between paraffin and high porosity open-cell metal foam, J. Heat Transfer 140 (2018).
[35] Y. Yao, H. Wu, Interfacial heat transfer in metal foam porous media (MFPM) under steady thermal conduction condition and extension of Lemlich foam conductivity theory, Int. J. Heat Mass Transf. 169 (2021) 120974.
[36] C. Zhao, J. Wang, Y. Sun, S. He, K. Hooman, Fin design optimization to enhance PCM melting rate inside a rectangular enclosure, Appl. Energy 321 (2022) 119368.
[37] Y. Yao, H. Wu, Macroscale modeling of solid–liquid phase change in metal foam/paraffin composite: effects of paraffin density treatment, thermal dispersion, and interstitial heat transfer, J. Therm. Sci. Eng. Appl. 13 (2021).
[38] H. Zheng, C. Wang, Q. Liu, Z. Tian, X. Fan, Thermal performance of copper foam/paraffin composite phase change material, Energ. Conver. Manage. 157 (2018) 372–381.
[39] A.I.N. Korti, H. Guellil, Experimental study of the effect of inclination angle on the paraffin melting process in a square cavity, J. Storage Mater. 32 (2020) 101726.
[40] A. Agarwal, R. Sarviya, Characterization of commercial grade paraffin wax as latent heat storage material for solar dryers, Mater. Today Proc. 4 (2017) 779–789.
[41] N. Ukrainczyk, S. Kurajica, J. Šipušić, Thermophysical comparison of five commercial paraffin waxes as latent heat storage materials, Chem. Biochem. Eng. Q. 24 (2010) 129–137.
[42] O.C. Zienkiewicz, R.L. Taylor, P. Nithiarasu, The Finite Element Method for Fluid Dynamics, Seventh ed., Butterworth-Heinemann, Oxford, 2014.
[43] D. Pepper, The Intermediate Finite Element Method: Fluid Flow and Heat Transfer Applications, Routledge, 2017.
[44] C.T. Kelley, Solving Nonlinear Equations with Newton's Method, SIAM, 2003.
[45] P. Deuflhard, Newton methods for nonlinear problems: affine invariance and adaptive algorithms, Springer Science & Business Media, 2005.
[46] M. Bollhöfer, O. Schenk, R. Janalik, S. Hamm, K. Gullapalli, State-of-the-art sparse direct solvers, Parallel Algorithms Comput. Sci. Eng. (2020) 3–33.
[47] M. Bollhöfer, A. Eftekhari, S. Scheidegger, O. Schenk, Large-scale sparse inverse covariance matrix estimation, SIAM J. Sci. Comput. 41 (2019) A380–A401.
[48] M. Bouzidi, M. Sheremet, K. Shank, S. Tiari, M. Ghalambaz, Charging and discharging heat transfer improvement of shell-tube storage utilizing a partial layer of anisotropic metal foam, J. Storage Mater. 79 (2024) 109948.
[49] A. Alasmari, H.S.S. Aljibori, F. Alimi, M. Bouzidi, M.S. Islam, S. Yazdani, M. Ghalambaz, A shell-tube latent heat thermal energy storage: Influence of metal foam inserts in both shell and tube sides, Int. Commun. Heat Mass Transfer 159 (2024) 107992.
[50] Shafi, jana; Younis, Obai; Tiari, Saeed; Ghalambaz, Mohammad (2025), "Artificial intelligence – Numerical study of melting and solidification heat transfer in a bundle of petal tubes embedded in metal foam: Dataset", Mendeley Data, V1, https://doi.org/10.17632/8965c9hpxr.1.
[51] Scikit-Learn, sklearn.preprocessing. StandardScaler, in, Vol. 2023, Scikit-Learn., 2023.
[52] I.K.M. Jais, A.R. Ismail, S.Q. Nisa, Adam optimization algorithm for wide and deep neural network, Knowledge Eng. Data Sci. 2 (2019) 41–46.